

A Statistical Study of Rest-frame Optical Emission Properties in Luminous Quasars at $2.0 \leq z \leq 2.5$ ¹

D. H. McIntosh^{2,3}, M. J. Rieke², H.-W. Rix²

C. B. Foltz⁴

R. J. Weymann⁵

ABSTRACT

We have obtained H -band spectra of 32 luminous quasars at $2.0 \leq z \leq 2.5$ with the Multiple Mirror Telescope. The sample contains 15 radio-loud quasars (RLQs) and 17 radio-quiet quasars (RQQs). We have measured emission line properties from the rest-frame wavelength range of approximately $\lambda\lambda 4500 - 5500$, by fitting the data with composite model spectra. Our analysis includes comparison of RLQs versus RQQs, as well as comparison between the broad-absorption-line quasar (BALQSO) and non-broad-absorption-line quasar (nonBALQSO) subsets of the RQQ sample. In addition, we calculated the complete correlation matrix of the measured properties. We combined our high redshift sample with the sample of 87 low redshift quasars from Boroson & Green (1992) to determine the luminosity and redshift dependences of the measured emission properties.

Our main results are: (1) The RLQ sample has significantly (at $> 97.2\%$ confidence) stronger $[\text{O III}]\lambda 5007$ emission than the RQQ sample, which favors scenarios including two populations of quasars that are intrinsically different. We are not aware of a unified model based upon orientation that can explain enhanced $[\text{O III}]$ emission with increased radio power. (2) The RLQ sample has significantly narrower (in full-width at half-maximum) $H\beta$ broad component line profiles than the RQQ sample. (3) At the sensitivity of our observations, there are no statistically significant ($> 95\%$) differences between the rest-frame optical emission line properties of the BALQSO and nonBALQSO subsamples. This result is consistent with the view that all RQQs

¹Observations reported here were obtained at the Multiple Mirror Telescope Observatory, a facility operated jointly by the University of Arizona and the Smithsonian Institution.

²Steward Observatory, University of Arizona, Tucson, AZ 85721

³E-mail: dmac@as.arizona.edu

⁴Multiple Mirror Telescope Observatory, University of Arizona, Tucson, AZ 85721

⁵Observatories of the Carnegie Institute of Washington, 813 Santa Barbara Street, Pasadena, CA 91101

have broad-absorption-line clouds with a small ($\sim 10 - 20\%$) covering factor and that differences between the two types are merely a function of viewing angle and covering factor. (4) The significant [O III] – Fe II anti-correlation found in lower redshift quasars holds at this higher redshift range; however, it is the [O III] emission in this relationship that appears to be related to the physical distinction between the RLQ and RQQ classes instead of the Fe II emission that distinguishes at low redshifts and luminosities. We also find significant relationships between (i) the [O III] emission strength and the radio power, the broad-emission-line widths, and the X-ray continuum shape; (ii) positive correlations relating the strength of optical Fe II emission to broad-emission-line widths and the shape of the ionizing continuum; and (iii) similar relations for the strength and width of the $H\beta$ emission. Many of these correlations have been found in lower redshift and luminosity studies. (5) We report a previously unknown luminosity and/or redshift dependence of the narrow-line-region velocity width over the range $0 < z < 2.5$, such that emission line widths *increase* with increasing luminosity. We confirm a similar dependence for the $H\beta$ broad line width. These findings may be evidence for a physical connection between the continuum and line-emitting regions at similar energies. Furthermore, we find a “Baldwin Effect” for the [O III] λ 5007 line in the RQQ-only sample over this same range in redshifts.

Subject headings: galaxies: active — infrared: quasars — line: profiles — quasars: emission lines — quasars: general

1. Introduction

Quasi-stellar objects (QSOs \equiv quasars) are among the most luminous objects in the Universe, thus they give us the unique opportunity to observe processes taking place at early epochs of the Universe. A “standard model” for QSOs has emerged where the continuum luminosity (up to $L \sim 10^{48}$ ergs s^{-1}) is primarily produced in an accretion disk surrounding a super-massive black hole. This model is supported by several points: (i) the mass of the central object is suggested by the Eddington limit $M_{Edd} = 8 \times 10^5 L_{44} M_{\odot}$ (where L_{44} is the luminosity in 10^{44} ergs s^{-1}), thus one would expect $M \sim 10^{10} M_{\odot}$ (Peterson 1997); (ii) continuum variability studies have shown conclusively that the continuum is produced in a very small region ($r \sim$ few light days $\sim 10^{16}$ cm, Peterson 1993); and (iii) the extreme energy output and tightly collimated radio jets that emerge from the nuclei of radio-loud QSOs suggest a strong gravitational source with large angular momentum, both defining qualities of an accretion fed giant black hole (Brotherton 1996).

One key to understanding the central engines of quasars lies in examining their local environment. As most of the power of QSOs is emitted in the ultraviolet (UV) to soft X-ray regime (Laor *et al.* 1997), this flux will photo-ionize the surrounding gas in physically distinct regions. The broad emission lines in quasar spectra are thought to originate from the photo-ionization of

dense ($n_e \approx 10^{11} \text{ cm}^{-3}$, Ferland *et al.* 1992), high velocity ($v_{FWHM} \lesssim 10^4 \text{ km s}^{-1}$) clouds that populate the unresolved broad-emission-line-region (BELR) within $r \sim 0.1 - 1.0 \text{ pc}$ of the nucleus (Kaspi *et al.* 1996). Line diagnostics indicate that the BELR ionized gas clouds have temperatures of a few 10^4 K . Since thermal and pressure broadening are negligible for the inferred density and temperature (Blandford & McKee 1982), the lines must be broadened by bulk motions of the BELR clouds (*e.g.* Woltjer 1959; and Burbidge & Burbidge 1967). Reverberation studies (*e.g.* Clavel *et al.* 1991; and Peterson *et al.* 1991) have shown a time-delayed response between emission line strengths and continuum variations, indicating a radially stratified ionization structure and confirming that the BELR is indeed photo-ionized (Baldwin 1997). A fairly successful model that reproduces the mean QSO broad emission spectrum and ties many of these details together, proposes that the BELR is an ensemble of locally optimally emitting clouds (LOCs) with a modest covering factor (Baldwin *et al.* 1995).

The narrow-line-region (NLR, $v_{FWHM} \sim 10^3 \text{ km s}^{-1}$), at $r \sim 1 \text{ kpc}$, is believed to be photo-ionized by continuum radiation extending from the Lyman edge to the soft X-rays (Wilson 1997). Forbidden transitions, such as $[\text{O III}]\lambda\lambda 4959, 5007$, dominate the NLR emission and are radiating near their critical densities (Filippenko & Halpern 1984), indicating NLR densities of $n_e \sim 10^3 \text{ cm}^{-3}$. Recent Hubble Space Telescope (HST) observations of a handful of local active-galactic-nuclei (AGN) have resolved the NLR and shown it to have a roughly bi-conical geometry (*e.g.* Wilson *et al.* 1993; Bower *et al.* 1995; and Simpson *et al.* 1996).

A significant issue in understanding the plethora of AGN “types” is the question of *intrinsic* vs. *orientation* differences. The radio-loud QSO (RLQ)/ radio-quiet QSO (RQQ) dichotomy is an important example of the intrinsic vs. orientation dilemma in QSO astronomy. Kellermann *et al.* (1989) originally defined the radio-to-optical ratio $R_{r-o} = \frac{F_\nu(5GHz)}{F_\nu(4400\text{\AA})}$ and called QSOs with $R_{r-o} > 10$ radio-loud. This ratio, regardless of specific radio and optical flux apertures, appears bimodal with an absence of objects in the $R_{r-o} = 1$ to 10 range (Kellermann *et al.* 1989; Visnovsky *et al.* 1992; Stocke *et al.* 1992; and Hooper *et al.* 1995). The distribution of QSOs at higher redshift ($1.8 < z < 2.5$) also appears bimodal in terms of the 5 GHz radio luminosity only (Miller, Peacock & Mead 1990). The fraction of RLQs ($\sim 10\%$) in optically selected samples does not evolve significantly from $z = 0.2$ to redshifts approaching 5 (Hooper *et al.* 1996). In terms of morphology, many RLQs have radio lobes and energetic jets of beamed radio emission extending to hundreds of kpcs, while similar radio features are absent in RQQs. This characteristic bright compact radio emission is thought to originate from non-thermal synchrotron sources due to the nearly flat slopes and typically high ($\sim 10^{11-12} \text{ K}$) brightness temperatures (Peterson 1997). Elvis *et al.* (1994) produced the mean spectral energy distributions (SEDs) for a set of RLQs and RQQs and showed that they have roughly the same SEDs from 1000\AA to $100\mu\text{m}$, but that the RLQs are ~ 1000 times brighter at radio wavelengths and ~ 3 times brighter in X-rays, compared to RQQs. RLQs also show a flatter, harder soft X-ray slope, and it is believed that this extra X-ray luminosity is due to a hard, non-thermal component produced by the inverse Compton scattering of radio emission along the associated jet (Elvis *et al.* 1994; and Green *et al.* 1995).

The physical process that is responsible for the difference in radio emission between RLQs and RQQs remains unknown. The spectral similarities at most wave-bands imply that the black hole mass and the accretion rate should be quite similar in RLQs and RQQs (Hooper *et al.* 1996). The angular momentum of the super-massive black hole might provide a potential difference such that large spin energy could produce powerful radio emission (Blandford 1990). Rapidly rotating massive black holes may form in the merger of two black holes of similar masses (Wilson & Colbert 1995). Alternatively, RLQs may constitute a short-lived phase during the lifetimes of all quasars (Wills 1996).

Other differences between RLQs and RQQs have been observed: (i) in rest UV emission line strengths (Corbin 1991; Francis, Hooper & Impey 1993, hereafter FHI93; Corbin & Francis 1994; Brotherton *et al.* 1994a); (ii) in rest UV line widths (Jackson & Browne 1991; Corbin 1991; FHI93; Wills *et al.* 1993; Corbin & Francis 1994; Brotherton *et al.* 1994a; Baker & Hunstead 1995; and Vestergaard, Wilkes & Barthel 1997); (iii) in optical rest-frame broad lines (Boroson & Green 1992 – hereafter BG92; and Corbin & Boroson 1996); and (iv) as stronger [O III] emission in RLQs (BG92; and Wills & Brotherton 1996).

Another important example of the intrinsic vs. orientation problem concerns the broad-absorption-line QSO (BALQSO) phenomenon. About 10% of optically selected QSOs have UV rest spectra showing deep, broad ($v_{FWHM} \lesssim 20,000 \text{ km s}^{-1}$) absorption lines extending blueward from the corresponding emission lines in the high ionization transitions of C IV λ 1549, Si IV λ 1400, N V λ 1240, and O VI λ 1035 (Green *et al.* 1995). In particular, the strength and proximity of the C IV absorption relative to its corresponding C IV λ 1549 emission line, provides the basis for determining the strength (BALnicity) of the BAL phenomenon in individual QSOs (Weymann *et al.* 1991; hereafter WMFH91). In addition, a small fraction ($< 10\%$) of BALQSOs, known as loBALs or Mg II BALQSOs, show additional broad-absorption-line (BAL) features in the low ionization species at Mg II λ 2798, Al II λ 1671, and Al III λ 1855, 1863 (WMFH91; and Peterson 1997).

It has been demonstrated that the rest-frame UV emission line properties of BALQSOs and radio quiet non-broad-absorption-line QSOs (nonBALQSOs) are quite similar (WMFH91). Furthermore, the total lack of radio loud BALQSOs (Stocke *et al.* 1992; except possibly 1556+3517 Becker *et al.* 1997) establishes a strong anti-correlation between luminous radio sources and the BALQSO phenomenon. This is consistent with current QSO unification theories that propose that BALQSOs do not form an intrinsically different class of objects from radio quiet nonBALQSOs. The standard unification model places an ensemble of BAL clouds in the neighborhood of the BELR of the “standard model”. Spectropolarimetry studies place the broad-absorption-line-region (BALR) location just exterior to the BELR at $r \sim 1 \text{ pc}$ (Cohen *et al.* 1995; and Glenn, Schmidt & Foltz 1994). Scattering constraints between the C IV emission and absorption establish a low covering factor, roughly equal to the BALQSO detection rate ($\sim 10\%$), for the BAL clouds (Hamann, Korista & Morris 1993). BALQSOs are known to be weak in X-ray flux (Turnshek 1984; Green *et al.* 1995 & 1996); therefore, a RQQ is classified a BALQSO when viewed through

the small angle containing the BAL clouds which may be sloughed off the surface of the accretion disk, thus any minor emission-line differences between BALQSOs and nonBALQSOs is due to obscuration associated with the BAL clouds. In this picture, any emission produced on larger spatial scales such as forbidden [O III] emission lines from the NLR should be isotropic in BALQSOs and radio quiet nonBALQSOs.

Assuming that [O III] emission is indeed an isotropic property, Boroson & Meyers (1992; see also Turnshek *et al.* 1994) argued that loBALs may represent a rare population of QSOs physically distinct from RQQs and hiBALs — the differences due to much larger (up to 100%, hence roughly spherically symmetric) BAL covering factors that would inhibit ionization of the narrow [O III] emitting gas. The strong N V λ 1240 absorption associated with the absence of Ly α emission in loBALs also suggests large covering factors (Peterson 1997). Others have argued for unification of both BALQSO types — suggesting the differences are the result of lines of sight through hot dust (Sprayberry & Foltz 1992; Hines & Wills 1995; Goodrich & Miller 1995; and Wills & Brotherton 1996), possibly due to ongoing nuclear starbursts (Lipari 1994).

In this paper, we have selected a sample of 32 very luminous QSOs with redshifts spanning the range $2.0 \leq z \leq 2.5$. This sample was magnitude limited ($V \lesssim 18.0$) so that sufficient signal-to-noise (S/N) near-infrared (NIR) H -band spectra could be obtained with a 4-meter class telescope. These observational parameters allowed us an unprecedented view of the rest-frame optical emission lines of high redshift and high luminosity quasars. The spectra were centered near the interesting H β , [O III] $\lambda\lambda$ 4959, 5007 and blended Fe II features. Consequently, we present the first detailed study of the important [O III] NLR emission at these redshifts, when the Universe was $\sim 75\%$ younger and QSOs were in their “heyday” — they existed in the largest numbers and the brightest QSOs were 10 – 100 times more luminous than their corresponding present-day counterparts. The recent advances of NIR spectrographs with adequate sensitivity and array size have just made these types of moderate resolution studies feasible. Until now, only a handful of very low resolution NIR spectra have been obtained for $z \sim 2$ QSOs (Carswell *et al.* 1991; Hill, Thompson & Elston 1993; and Baker *et al.* 1994).

From the rest-frame optical emission line properties, combined with continuum parameters from the radio, optical and soft X-ray band-passes, plus rest-frame UV emission line data, we can perform a complete high redshift QSO property correlation analysis similar to the important low redshift study carried out by BG92. Our selection of approximately equal numbers of RLQs (15) and RQQs (17) allows us to study the statistical differences between these types in terms of observed characteristics that have been previously poorly examined at high redshift. The same justification applies to our subsamples of BALQSOs (7) and radio quiet nonBALQSOs (10).

The organization of this paper is as follows: In §2 we describe the selection and observation of this sample. We also calculate and tabulate the continuum parameters: (i) the ratio of radio-to-optical flux; (ii) the rest-frame V band luminosity density; and (iii) the monochromatic soft X-ray luminosity density plus optical-to-X-ray spectral index. We compile the rest-frame UV

line widths and equivalent widths (EWs). In §3 we describe the raw data reduction procedures, the systemic redshift determination, the construction of a composite model spectrum and the fit of this model to the data, and the measurement of the emission line properties from the data. In §4 we calculate the Spearman Rank, and the Kendall τ (to check for consistency), correlation matrices for the measured and compiled rest-frame emission properties of our combined RLQ + RQQ sample. The significant results are compared to findings from the literature. In §5 we fit our model spectrum to BG92’s low redshift sample, then combine the results with the similar optical rest-frame measurements from our high redshift sample. We use this combined sample spanning the redshift range $0 < z < 2.5$ to determine the dependencies on rest-frame V band luminosity and/or redshift for each of the measured properties. In §6 we draw the RLQ and RQQ subsamples from our data and perform statistical tests to determine the differences in emission parameters between these. The significant results we find for the rest-frame optical wavelengths are added with rest-frame UV differences from the literature to test the validity of the proposed QSO model that RLQs and RQQs are separate classes of QSO. In §7 we perform the same analysis as §6 on the BALQSO and nonBALQSO subsets drawn from the RQQ sample. We use our findings to test the validity that BALQSOs are a subset of all RQQs and that observed differences are due to orientation coupled to coverage of the BAL material. We also note specific object-to-object spectral differences in light of the loBAL phenomenon. In §8 we summarize our results, and in §9 we discuss our results in the context of two simple models, one RLQ and the other RQQ.

2. Observations

A total of 32 QSOs brighter than $V = 18.0$ mag., with redshifts between $2.0 \leq z \leq 2.5$, were observed. The sample consists of 7 BALQSOs (5 from WMFH91), 10 nonBALQSOs, and 15 RLQs. One object, Q1148-001, has redshift $z = 1.980$ slightly out of our specified range and thus no $H\beta$ measurements were obtained.

All observations were made in the H -band with the long-slit near-IR spectrometer, FSPEC (Williams *et al.* 1993), at the 4.5-meter Multiple Mirror Telescope (MMT). FSPEC uses a 256×256 NICMOS3 HgCdTe array and a 75 grooves per millimeter low resolution grating providing a two-pixel resolution of about 700. Observations were taken through an $H(1.6\mu\text{m})$ filter at four positions along a $1.2''$ by $30''$ slit which produced an instrumental resolution of about 550 km s^{-1} and spectral coverage of about $0.30\mu\text{m}$. The limiting V magnitude corresponds to $H \sim 16$ mag. which allowed a $S/N \approx 10$ to be achieved in exposure times of a few hours. The slit was positioned along a line of constant azimuth for all observations and we attempted to observe at air masses less than 1.60. Spectra of atmospheric transmission standard stars, used to remove telluric atmosphere absorption features, were obtained at least twice a night for each object observed. Exposure times were typically between 960 and 7200 seconds. Observations were made over many nights between November 1993 and April 1996. The log of observations is presented in Table 1. Columns (3) and (4) contain the published apparent V -band magnitude

and redshift, respectively. Column (5) lists the systemic redshift measured from the forbidden narrow [O III] λ 5007 line in this study (see §3.1). Additional photometric properties compiled from the literature are presented in Table 2. Column (2) classifies each QSO as radio-quiet (RQ) or BAL (BALQSO) such that $\log(R') < 1$, or radio-loud RL ($\log(R') > 1$). Column (3) gives the logarithm of R' , the ratio of the *observed* radio (5 GHz) flux density to the *observed* optical V -band flux density assuming zero magnitude in V is 3880 Jy (Johnson 1966). Though this R' parameter differs slightly from other radio-to-optical (R) parameters normally used to classify AGN (see for example Kellermann *et al.* 1989, Hooper *et al.* 1995, Stocke *et al.* 1992), the resultant bimodal distribution and classifications are consistent with those from the literature. Column (4) lists the 5 GHz flux reference(s), in some cases $F_{5\text{GHz}}$ was extrapolated from $F_{1.4\text{GHz}}$, $F_{4.85\text{GHz}}$, or $F_{8.4\text{GHz}}$ assuming $F_\nu \propto \nu^{-\frac{1}{2}}$ over radio frequencies (FHI93). Column (5) gives the logarithm of the luminosity density (in $\text{ergs s}^{-1}\text{Hz}^{-1}$) emitted at rest-frame V given by

$$L_\nu(V) = 4\pi D_L^2(z) F_\nu(H) (1+z)^{-1}. \quad (1)$$

$$D_L(z) = \frac{2cz}{H_0 g} \left(1 + \frac{z}{g}\right) \quad (2)$$

is the luminosity distance from Hall *et al.* (1997), with

$$g = 1 + \sqrt{1 + 2zq_0}, \quad (3)$$

c is the velocity of light, and $z = z_{\text{sys}}$ is the systemic redshift measured in this study. $F_\nu(H)$ is the observed H -band flux density (in $\text{ergs cm}^{-2} \text{s}^{-1} \text{Hz}^{-1}$) derived from H -band magnitudes and assuming zero magnitude in H is 1075 Jy (Campins, Rieke & Lebofsky 1985). Note that $\frac{\lambda_H}{\lambda_V} \approx 1 + \langle z \rangle$, and hence no K-corrections were necessary. Following BG92 we adopted an $H_0 = 50 \text{ km s}^{-1} \text{Mpc}^{-1}$ and $q_0 = 0.1$ cosmology throughout this paper. Columns (6) and (7) list the H -band magnitude and its reference. Column (8) gives the logarithm of the monochromatic soft X-ray luminosity density (in $\text{ergs s}^{-1}\text{Hz}^{-1}$) emitted at rest-frame 2 keV given by

$$L_\nu(2\text{keV}) = \sqrt{2\pi} D_L^2(z) F_\nu(1\text{keV}) \sqrt{1+z}, \quad (4)$$

where $F_\nu(1\text{keV})$ is the monochromatic (1 keV) flux density (in $\text{ergs cm}^{-2} \text{s}^{-1} \text{Hz}^{-1}$) derived from the *observed* flux density and assuming $F_\nu \propto \nu^{-\frac{3}{2}}$ over soft X-ray frequencies (Wilkes *et al.* 1994). The factor of root $(1+z)$ is related to the difference between the frequency corresponding to 1 keV and the *observed* frequency. Column (9) contains the mean spectral slope α_{ox} between the rest-frame optical (V -band) and rest-frame 2 keV soft X-ray emission. This spectral index is defined such that $L_\nu \propto \nu^{-\alpha_{ox}}$, or

$$\alpha_{ox} = -\frac{1}{a} \log \frac{L_\nu(2\text{keV})}{L_\nu(V)}, \quad (5)$$

where the constant $a = 2.948$ is the logarithm of the ratio of 2 keV to V -band frequencies. The luminosity densities, $L_\nu(V)$ and $L_\nu(2\text{keV})$, are from equations (1) and (4). Column (10) lists the soft X-ray references.

Table 1. Log of Observations

Object Name	Other Name	V^a (mag.)	z_{lit}^b	z_{sys}	RA(1950.0) ^c	Dec(1950.0) ^c	Date(s)	t_{exp} (sec.)
Q0043+008	UM275	17.	2.143	2.146	00h43m39.59s	+00°48′02″40	1993 Nov 29	3360
...	1993 Nov 30	3360
Q0049+007	UM287	17.8	2.268	2.279	00h49m28.43s	+00°45′11″30	1994 Sept 22	4800
Q0049+014	UM288	17.	2.310	2.307	00h49m59.56s	+01°24′23″30	1993 Nov 30	4800
Q0109+022	UM87	17.8	2.350	2.351	01h09m42.31s	+02°13′53″1	1994 Sept 22	4080
Q0123+257	4c25.05	17.5	2.358	2.370	01h23m57.26s	+25°43′27″88	1995 Nov 10	5040
Q0153+744	...	16.0	2.338	2.341	01h53m04.33s	+74°28′05″58	1994 Nov 17	2880
...	1995 Nov 2	1920
...	1995 Nov 6	3600
Q0226-104	...	17.0	2.256	2.268	02h26m00s	-10°24′0	1993 Nov 29	3360
Q0226-038	PHL1305	16.96	2.066	2.073	02h26m22.10s	-03°50′58″98	1994 Jan 31	4320
Q0421+019	...	17.04	2.055	2.056	04h21m32.67s	+01°57′32″70s	1993 Nov 30	5760
Q0424-131	...	17.5	2.165	2.168	04h24m47.85s	-13°09′33″40	1994 Jan 29	4080
Q0552+398	...	18.	2.365	2.363	05h52m01.40s	+39°48′21″94	1995 Nov 10	4680
Q0836+710	4c71.07	16.5	2.170	2.218	08h36m21.54s	+71°04′22″54	1993 Nov 29	4320
...	1993 Nov 30	4680
Q0842+345	CSO203	17.	2.126	2.163 ^d	08h42m30.37s	+34°31′41″0	1994 Jan 29	6240
...	1995 Mar 19	5760
Q1011+091	...	17.8	2.268	2.305 ^d	10h11m03.35s	+09°06′19″90	1993 Nov 30	4320
...	1994 Apr 30	960
...	1995 Mar 19	4320
Q1104-181	HE1104-1805A	16.2	2.319	2.318	11h04m04.95s	-18°05′10″07	1996 Apr 3	4200
Q1148-001	UM458	17.14	1.980	1.980	11h48m10.13s	-00°07′13″01	1996 Apr 7	7200
Q1158-187	Pox42	16.93	2.453	2.462 ^d	11h58m11.27s	-18°43′02″70	1995 Apr 10	5280
Q1222+228	Ton1530	15.49	2.048	2.058	12h22m56.58s	+22°51′49″00	1994 Apr 29	3840
Q1225+317	Ton0618	15.84	2.219	2.226 ^d	12h25m55.94s	+31°45′12″60	1994 May 20	1920
Q1228+077	...	17.59	2.391	2.389	12h28m48.02s	+07°42′26″40	1994 May 22	3120
Q1246-057	...	16.73	2.236	2.243 ^d	12h46m38.69s	-05°42′58″9	1994 May 26	2880
...	1995 Mar 19	3840
Q1247+267	PG1247+267	15.8	2.043	2.042	12h47m39.09s	+26°47′27″10	1994 Apr 29	2400
Q1309-056	...	17.44	2.188	2.220 ^d	13h09m00.75s	-05°36′43″40	1994 Apr 30	6240
...	1995 Mar 19	4320
Q1331+170	...	16.71	2.084	2.097	13h31m10.10s	+17°04′25″0	1996 Apr 1	2880
Q1346-036	...	17.27	2.349	2.362	13h46m08.32s	-03°38′30″80	1994 May 21	1440
...	1994 May 22	2760
...	1994 May 26	3840
Q1416+091	...	17.0	2.015	2.017	14h16m23.30s	+09°06′14″0	1994 Apr 29	4800
...	1995 Mar 19	3840
Q1435+638	...	15.	2.068	2.066	14h35m37.25s	+63°49′35″97	1996 Apr 6	6240
Q1448-232	...	16.96	2.215	2.220	14h48m09.31s	-23°17′11″30	1996 Apr 7	5760
Q1704+710	...	17.5	2.015	2.010	17h05m00.60s	+71°01′34″0	1994 May 26	3360
...	1994 Sept 22	2160
Q2212-179	...	18.3	2.280	2.228	22h12m48.30s	-17°59′03″1	1993 Nov	30
...	1994 Nov 15	3120
...	1994 Nov 17	4800
Q2251+244	4c24.61	17.8	2.327	2.359	22h51m44.57s	+24°29′23″80	1994 Sept 22	4320
...	1995 Nov 3	7080
Q2310+385	...	17.5	2.170	2.181	23h10m36.18s	+38°31′22″69	1993 Nov 29	4440

^aV-band magnitudes from Hewitt & Burbidge 1993; except for Q0226-104 and HE1104-1805A from NED; and Q0421+019, Q1148-001, Q1158-187, Q1228+077, Q1331+170, and Q1346-036 from Adam 1985.

^bPublished redshifts from Hewitt & Burbidge 1993; except for Q0226-104 from WMFH91; and HE1104-1805A from Wisotzki *et al.* 1993.

^cEpoch 1950.0 coordinates from NED.

^dUncertain measurement due to low [O III] EW and/or poor S/N spectrum.

Table 2. Photometric Properties

QSO	Type	$\log(R')$	Refs. ^{a,d}	$\log(L_\nu(V))$ (ergs s ⁻¹ Hz ⁻¹)	H (mag.)	Refs. ^b	$\log(L_\nu(2\text{keV}))$ (ergs s ⁻¹ Hz ⁻¹)	α_{ox}	Refs. ^{c,d}
Q0043+008	BAL	0.824	1,2	32.24	15.26	12 ^h	< 27.30	< 1.675	17 ⁱ
Q0049+007	RQ	< 0.230	3 ^e	32.08	15.79	12	26.84	1.777	18
Q0049+014	RQ	< 0.325	4 ^f	32.30	15.26	12 ^h	28.16	1.405	18
Q0109+022	RQ	0.133	3 ^e	32.24	15.46	12	< 28.26	< 1.350	18
Q0123+257	RL	3.393	5,6	32.13	15.76	12 ^h	28.84	1.115	19 ^j
Q0153+744	RL	2.990	5,7	32.72	14.26	12 ^h	28.40	1.464	19 ^j
Q0226-104	BAL	< -0.229	2	32.57	14.55	13	< 27.55	< 1.703	17 ⁱ
Q0226-038	RL	3.046	6	32.22	15.22	12 ^h	28.45	1.280	18
Q0421+019	RL	3.090	6	32.18	15.30	12 ^h
Q0424-131	RL	2.864	6,8	32.05	15.76	12 ^h	27.98	1.379	18
Q0552+398	RL	4.344	5	31.92	16.26	12 ^h	29.12	0.951	19 ^j
Q0836+710	RL	3.425	5,7	32.47	14.76	12 ^h	29.57	0.983	19 ^j ;20 ^j
Q0842+345	BAL	< 0.325	4 ^f	32.24	15.26	12 ^h
Q1011+091	BAL	< 0.008	2	32.28	15.32	13
Q1104-181	RQ	< 0.005	4 ^f	32.63	14.46	12 ^h	29.05	1.213	21 ^j
Q1148-001	RL	3.546	5,6,7	32.06	15.53	12	28.60	1.173	22 ⁱ
Q1158-187	RQ	< 0.297	4 ^f	32.39	15.19	12 ^h
Q1222+228	RQ	0.668	1,9	32.58	14.3	14	28.29	1.457	18
Q1225+317	RL	2.276	10 ^g ;11 ^g	32.69	14.20	15	28.53	1.413	19 ^j
Q1228+077	RL	2.003	11 ^g	32.10	15.85	12 ^h	28.33	1.278	18
Q1246-057	BAL	0.057	2	32.11	15.67	13	26.93	1.758	17 ⁱ
Q1247+267	RQ	-0.269	9	32.66	14.1	14	28.42	1.437	19 ^j
Q1309-056	BAL	< -0.534	2	32.11	15.65	13	27.90	1.428	18
Q1331+170	RL	2.909	10 ^g ;11 ^g	32.53	14.49	12	28.17	1.477	18
Q1346-036	RQ	< 0.433	4 ^f	32.22	15.53	12 ^h	< 28.13	< 1.386	18
Q1416+091	RQ	< 0.325	4 ^f	32.18	15.26	12 ^h
Q1435+638	RL	2.498	5,7	33.00	13.26	12 ^h	< 28.31	< 1.592	19 ^j
Q1448-232	RL	2.687	6	32.42	14.87	16	< 28.47	< 1.342	18
Q1704+710	RQ	< 0.525	4 ^f	31.98	15.76	12 ^h
Q2212-179	BAL	< 0.250	2	32.32	15.14	12	28.59	1.265	22 ⁱ
Q2251+244	RL	3.446	6,8	32.00	16.06	12 ^h	28.75	1.104	19 ^j
Q2310+385	RL	3.110	10 ^g ;11 ^g	32.05	15.76	12 ^h

^aThe 5 GHz flux references.

^bThe H -band magnitude references.

^cThe soft X-ray monochromatic (1 keV) flux density references.

^dMultiple references indicate that the value is an average.

^eReference contained 8.4 GHz fluxes.

^fReference contained 1.4 GHz fluxes.

^gReference contained 4.85 GHz fluxes.

^hCalculated H magnitudes from an average color $(V - H) = 1.74$, derived from a sample of 53 QSOs within our redshift range, supplied by Hewett & Foltz (1997).

ⁱDerived result from luminosity density for a $q_0 = 0.5$ cosmology.

^jDerived $F_\nu(1\text{keV})$ from ROSAT flux integrated between 0.1 and 2.4 keV, assuming $f_\nu \propto \nu^{-1.5}$.

References. — (1) Barvainis *et al.* 1996; (2) Stocke *et al.* 1992; (3) Hooper *et al.* 1995; (4) Condon *et al.* 1996 (NVSS); (5) Johnston *et al.* 1995; (6) Wright & Otrupcek 1990 (Parkes Survey); (7) Stickel *et al.* 1994; (8) Lonsdale *et al.* 1993; (9) Kellermann *et al.* 1989; (10) Gregory & Condon 1991 (GB87 Survey); (11) Gregory *et al.* 1996 (GB6 Survey); (12) Hewett & Foltz 1997; (13) Rieke & Weymann 1995; (14) Neugebauer *et al.* 1987; (15) Sitko *et al.* 1982; (16) Hyland & Allen 1982; (17) Green & Mathur 1996; (18) Wilkes *et al.* 1994; (19) Brinkmann *et al.* 1997; (20) Schartel *et al.* 1996; (21) Reimers *et al.* 1995; (22) Green *et al.* 1995.

3. Data Reduction

Basic reduction of the science frames, using standard IRAF⁶ routines, included subtraction of the dark current and offset level, and division by normalized flatfield frames obtained with the same grating and wavelength settings as the object frames. Fewer than 1% of the array’s pixels were bad and these were removed. In the near-IR, OH airglow is particularly unstable. Thus sky subtraction was performed by interactively scaling the background images before subtracting. The background is merely the adjacent frames with the QSO at another position along the spectrometer slit. The individual frames were aligned and their relative weights were calculated interactively. With this information the frames were combined into a single, averaged frame. Once combined, the residual OH emission, usually from the three strong Q-branch features, was removed by subtracting a background residual frame produced by median combining the 100 columns centered on the slit in the object frame. One dimensional sky-subtracted spectra were extracted from the final averaged frames using a spatial width defined by $\sim 90\%$ FWHM (full-width at full-maximum) of the flux centered on the nucleus. Each spectrum was divided by the reduced spectrum of its corresponding standard to remove atmospheric absorption features. We chose spectral type A0V – G3V standards, with close proximity to the sample QSOs, from the Bright Star Catalogue (Hoffleit & Jaschek 1982). The spectra were then wavelength calibrated using atmospheric OH airglow lines and rebinned to a linear dispersion of $\sim 11.5 \text{ \AA}$ per pixel. For objects that were observed on multiple nights, a single combined spectrum was produced from a S/N weighted average of the reduced spectra from separate observations. The completely reduced spectra of the 32 QSOs are shown, along with their best fit model (see §3.2), in each top panel of Figure 1. The horizontal axis is the rest-frame wavelength (in \AA), and the vertical axis is an arbitrary flux level that is normalized to the square of the S/N. We did not attempt to calibrate the spectra to an absolute flux scale since the narrowness of the slit did not provide a sufficient enough aperture for collecting the entire nuclear flux from each QSO.

3.1. Systemic Redshift Determination

To measure the systemic redshift z_{sys} of each QSO, the spectra were boxcar smoothed by 3 pixels and the upper half of the [O III] $\lambda 5007$ line was fit by a Gaussian, except in the case of six objects (Q0842+345, Q1011+091, Q1158-187, Q1225+317, Q1246-057, and Q1309-056). Due to the low [O III] EW and the poor S/N of these spectra, the peak or centroid of the [O III] $\lambda 5007$ line was used, except for Q1246-057 which had no [O III] emission and thus the peak of the $H\beta$ line was used. Both Q1225+317 and Q1246-057 have strong, blended Fe II emission and the location of minima of this emission blueward of $H\beta$ ($\lambda_{\text{min}} \sim 4750 \text{ \AA}$) and redward of [O III] ($\lambda_{\text{min}} \sim 5090 \text{ \AA}$) gave an approximate confirmation of the redshifts for these objects. Finally, the spectra were

⁶IRAF is distributed by the National Optical Astronomical Observatories, which are operated by AURA, Inc. under contract to the NSF.

moved to the rest-frame by dividing their linear dispersion by $(1 + z_{\text{sys}})$ and then transformed to a linear logarithmic wavelength scale with a dispersion of 3.5 \AA per pixel necessary for compatibility with the fitting routine. The measured systemic redshifts are presented in column (5) of Table 1.

3.2. Fitting the Spectra with a Multi-component Model

The spectral features around the $H\beta$ and $[\text{O III}]\lambda\lambda 4959, 5007$ complex, as well as the continuum level, are complicated by the presence of many blended Fe II emission lines. In particular, there are two broad features at $\lambda\lambda 4450 - 4700$ and $\lambda\lambda 5150 - 5350$, and a strong multiplet (42) of three lines at $\lambda\lambda 4924, 5018, 5169$. As BG92 showed, it is necessary to subtract this Fe II emission from the spectra before accurate measurements of the $H\beta$ and $[\text{O III}]\lambda 5007$ lines can be obtained, and before the continuum can be defined. Instead of subtracting a variety of different width and strength Fe II templates, looking for the best fit “by eye”, and then removing the continuum by fitting a low order polynomial to the regions where there was Fe II contamination (BG92), we developed a least squares χ^2 minimization routine that simultaneously fit for line strength, width and continuum slope, thereby producing the best fit model spectrum for each QSO. This application was particularly favorable given the low S/N of our data set.

Our spectral model was the composite of several templates. First was an object-specific Fe II emission template (originally from I Zw 1, courtesy BG92), broadened by a Gaussian of the same full-width at half-maximum (FWHM) as observed for the $\text{C IV}\lambda 1549$ broad emission line taken from the literature. Due to the high redshift of our sample of QSOs, the $\text{C IV}\lambda 1549$ emission line was the observed permitted broad line with the least amount of contamination by other species. Thus, we tacitly assumed that the broad component of both C IV and Fe II were emitted from roughly the same region and therefore have the same line width. We assumed, as did BG92, that the relative strengths of the Fe II lines, within each multiplet and between multiplets, were the same for all QSOs. For the two cases, Q1416+091 and Q1704+710, where the C IV line width was not available, we used the published $\text{C III}\lambda 1909$ line width with the same basic assumptions instead. For one of the seven BALQSOs (Q0226-104), we used a C IV FWHM defined by the product of doubling the red HWHM (half-width at half-maximum) to account for possible biasing by the broad absorption trough. The other six BALQSOs were all found to have absorption troughs *detached* from the emission line.

The Fe II template was combined with sets of templates representing hydrogen Balmer and $[\text{O III}]$ emission, as well as a set of 3 orthonormal vectors (flat, positively sloped, and negatively sloped) that reproduced the sloped continuum approximated by a first order power-law. There were 5 templates for hydrogen Balmer emission, each one a spectrum of two Gaussian line profiles, $H\gamma\lambda 4340$ and $H\beta\lambda 4861$ with the ratio of $H\beta = 1.70 \times H\gamma$ from the composite QSO spectrum of Francis *et al.* (1991). The $[\text{O III}]$ emission was represented as 5 templates as well, each one a spectrum of two Gaussian lines, $\lambda 5007$ and $\lambda 4959$, with a relative strength ratio of 3 to 1 given by the ratio of the two transition probabilities from the 1D level (Osterbrock 1989). In AGN, narrow

forbidden lines (such as [O III]) are generally found to have widths of several hundred to a few thousand km s^{-1} FWHM, and broad permitted lines (such as $\text{H}\beta$) are seen with widths up to 10^4 km s^{-1} FWHM (see for instance Peterson 1997). The minimum width used for the hydrogen Balmer and the [O III] template sets was equal to FSPEC’s instrumental line-width of 550 km s^{-1} FWHM. From initial test fitting of our sample we found that a maximum template width for [O III] of 2580 km s^{-1} FWHM was necessary to fit the broadest forbidden lines (those of Q1158-187). The three remaining [O III] templates have widths intermediate between the minimum and maximum values by factors of $\frac{1}{\sqrt{2}}$ of the maximum (912, 1290 and 1820 km s^{-1} FWHM). For the hydrogen Balmer broad lines, we chose a maximum template width of 10320 km s^{-1} FWHM, which is four times the maximum narrow line width, as well as nearly equal to the broadest C IV line width from the literature (10350 km s^{-1} for Q1225+317). The remaining Balmer templates have intermediate widths that are factors of $\frac{1}{2}$ below the maximum (1290, 2580 and 5160 km s^{-1} FWHM). We did not include the [O III] $\lambda 4363$ line, nor the He II $\lambda 4686$ line, in our templates. These lines fall within the spectral range of our sample but were too weak to detect given the low S/N of the observations.

A further complication in constructing Balmer template sets for each QSO in our sample was the nonzero difference between z_{sys} determined by the [O III] $\lambda 5007$ line and the redshift from the $\text{H}\beta$ line. This effect is of obvious importance — for example, determining the center-of-mass rest-frame of QSOs and of their host galaxies is crucial in estimating the inter-galactic radiation field via the Proximity Effect. The redshift difference between the NLR and the BELR in this sample will be addressed in a separate paper (McIntosh *et al.* 1999, in preparation). To correct for this effect in our fitting routine, we measured the individual $\text{H}\beta$ line centers by direct examination of each boxcar smoothed, rest-frame spectrum, then we used this value to shift each object’s set of 5 Balmer templates to match its measured line center.

A total of 14 component templates (1 Fe II, 5 [O III], 5 Balmer and 3 power-law) make up our model spectrum. To have complete spectral coverage of our entire sample, each template spanned the range from $4196 - 5855 \text{ \AA}$, except for the Fe II template which began at 4250 \AA . Furthermore, each template was linearly rebinned to a logarithmic wavelength scale (3.5 \AA per pixel dispersion) over a total of 475 pixels.

Construction of each best fit model spectrum was done by simultaneously fitting, in pixel space, a linear combination of the minimum number of template spectra to the object spectrum. To do this we adapted a non-negative least-squares routine (see Rix *et al.* 1995) that minimizes the goodness-of-fit parameter

$$\chi^2 = \sum_{i=1}^N \left[\frac{1}{\sigma(x_i)} \left(y(x_i) - \sum_{k=1}^m a_k T_k(x_i) \right) \right]^2. \quad (6)$$

First the set of $m = 14$ templates T_k were trimmed to match the wavelength range (same initial pixel x_1 and number N of pixels) for each individual object spectrum y . The object and templates were weighted by the object spectrum noise $\sigma(x_i) \simeq \sqrt{y(x_i)}$ (Poisson statistics). Then an iterative

process multiplied the templates by scalar coefficients a_k , calculated the linear combination (composite model) and compared it to the input QSO spectrum until the optimum fit was obtained. The optimum fit was such that the reduced chi-squared

$$\chi_{\nu}^2 = \frac{\chi^2}{N_{\text{d.o.f.}}} \approx 1, \quad (7)$$

where the number of degrees of freedom is $N_{\text{d.o.f.}} = N - m'$, the total number of pixels minus the number of templates used (those with nonzero coefficients a_k).

The final composite model spectrum was comprised of four components - broad $\text{H}\beta$ emission, narrow $[\text{O III}]$ emission, broad Fe II emission and a sloped continuum. For the $\text{H}\beta$ and $[\text{O III}]$ components, a linear combination of Gaussians at equivalent line centers, over a range of widths, resulted in a symmetric, pseudo-Lorentzian line profile for $\text{H}\beta$ and a blended, double line profile for $[\text{O III}]\lambda\lambda 4959, 5007$. The summation of many blended broad lines gave the Fe II component the look of a high order polynomial continuum. The sloped continuum was a superposition of the flat continuum template and one of the two sloped, either negative or positive, templates. The best fit model and its individual components for each QSO are plotted in the bottom panels of Figure 1. The parameters used to determine each best fit model are presented in Table 3. Column (2) lists the Fe II template FWHM in km s^{-1} . Column (3) gives the Balmer template $\text{H}\beta$ line center in \AA . The number m' of templates used to construct the model spectrum is given in column (4). The final best fit χ_{ν}^2 and the number of degrees of freedom $N_{\text{d.o.f.}}$ are tabulated in column (5). Column (6) cites the reference(s) of the C IV $\lambda 1549$ line width used to broaden each Fe II template.

Table 3. Best Fit Template Specifications

QSO	Fe II FWHM (km s ⁻¹)	Balmer Center (Å)	m'^a	χ^2_ν ($N_{d.o.f.}$)	Refs. ^{b,c}
Q0043+008	3000	4870	10	1.005(232)	1
Q0049+007	8300	4864	8	1.008(247)	2 ^d
Q0049+014	8200	4865	9	0.999(226)	2 ^d
Q0109+022	5260	4859	7	1.001(217)	3
Q0123+257	4700	4865	11	1.011(238)	1
Q0153+744	5250	4872	9	1.001(251)	4
Q0226-104	6772	4869	9	1.000(226)	5 ^e
Q0226-038	4500	4864	10	0.992(259)	1, 6, 7, 8
Q0421+019	5100	4868	10	1.003(254)	9
Q0424-131	2820	4865	11	1.000(251)	7, 8
Q0552+398	3000	4870	7	1.003(222)	2 ^d
Q0836+710	6740	4858	8	1.001(250)	4
Q0842+345	6800	4862	9	0.998(266)	10 ^d
Q1011+091	10000	4851	8	1.007(261)	1
Q1104-181	6400	4870	9	0.996(197)	11 ^d
Q1148-001	2740	4861	9	1.000(248)	1, 7, 8
Q1158-187	4045	4847	8	0.999(213)	12
Q1222+228	4840	4857	10	0.998(252)	1, 8, 13 ^d
Q1225+317	10350	4864	7	1.000(258)	1, 8
Q1228+077	4000	4861	8	1.003(235)	1
Q1246-057	5000	4861	9	1.000(253)	1
Q1247+267	3610	4875	10	1.001(250)	1, 8, 13 ^d
Q1309-056	5000	4871	9	1.004(250)	1
Q1331+170	5210	4861	7	0.999(262)	1, 8, 14
Q1346-036	10000	4874	9	1.000(230)	1
Q1416+091	7500 ^f	4867	8	0.997(250)	7
Q1435+638	4200	4872	9	1.001(267)	7, 8
Q1448-232	3610	4874	10	0.997(267)	12
Q1704+710	6000 ^f	4871	10	1.013(254)	7
Q2212-179	3000	4863	8	0.998(256)	1
Q2251+244	6600	4855	9	1.000(197)	15
Q2310+385	4300	4875	9	0.990(251)	16 ^d

^aThe number of non-zero weighted templates, out of a total possible 14, used to achieve the best fit model spectrum.

^bThe C IV λ 1549 line width references.

^cMultiple references indicate the use of an average line width.

^dThe C IV λ 1549 line width was measured directly off the published spectrum.

^eFWHM of C IV line derived from red HWHM.

^fUsed the C III] λ 1909 line width since no C IV λ 1549 data was available.

References. — (1) Turnshek 1984; (2) Wolfe *et al.* 1986; (3) Schneider *et al.* 1994; (4) Lawrence *et al.* 1996; (5) WMFH91; (6) Tytler & Fan 1992; (7) Brotherton *et al.* 1994a; (8) Wills *et al.* 1993; (9) Baldwin *et al.* 1989; (10) Thompson *et al.* 1989; (11) Wisotzki *et al.* 1993; (12) Ulrich 1989; (13) Sargent *et al.* 1988; (14) Corbin 1992; (15) Corbin 1991; (16) Wills 1997.

3.3. Deriving Emission Line Properties from the Model

We derived emission line properties directly from the individual components of each composite model spectrum. Since the model represented the best fit to the rest-frame spectrum, all calculated emission line properties refer to the rest-frame. The EWs in this paper were measured relative to the fitted continuum component represented by the sloped line in the bottom panels of Figure 1. From the $H\beta$ and [O III] components, the strength (EW in Å) and width (FWHM in km s^{-1}) of the $H\beta$ and [O III] λ 5007 lines were calculated. In the case of the blended [O III] λ 4959, 5007 emission, the EW of the [O III] λ 5007 line was equal to $\frac{3}{4}$ the total EW of [O III] based on the known line ratio. In a few cases a small negative correction, arising from Brackett absorption lines in the telluric standard, was applied to the [O III] λ 5007 EW. In no case was this correction > 3.5 Å. For both $H\beta$ and [O III] λ 5007 the symmetry of the line profiles allowed the extrapolation of both the strength and the width of a line by calculating either the redward or blueward half and doubling it. This method was used for those QSOs with an $H\beta$ line too close to the blue edge of the spectrum, or conversely for those with [O III] λ 5007 too close to the red edge. The FWHM of $H\beta$ measured from the composite model represented the *total*, narrow plus broad components, line width ($H\beta_{\text{tot}}$ FWHM). For five objects (Q0049+007, Q1011+091, Q1158-187, Q1704+710 and Q2310+385) this quantity may have been underestimated. In these cases the line profile of the $H\beta$ component had a narrow spike on top of a broad hump due to the fitting routine possibly fitting noise with the narrowest Balmer template. A *relative* strength of the Fe II emission was determined by measuring the EW of the blended line complex between 4810 and 5090 Å. This spectral range was chosen since it encompasses the $H\beta$ and [O III] λ 4959, 5007 emission features. The width of the *broad* component of the $H\beta$ line ($H\beta_{\text{broad}}$ FWHM) was derived by fitting a single Gaussian to the component of the line profile defined by the relative flux $\leq \frac{3}{4}$ of the maximum. We separated the actual $H\beta$ emission by subtracting the other three best fit model components ([O III] λ 5007, Fe II and continuum) from the original spectrum. Then we used the Levenberg-Marquardt nonlinear χ^2 minimization method (see Press *et al.* 1992) to produce the fit and calculate the broad component FWHM as well as its line center. As an example, the reduced rest-frame spectra with extracted $H\beta$ lines, for a RLQ (Q0424-131), a RQQ (Q1346-036) and a BALQSO (Q1246-057), are shown in Figure 2.

The measured emission line properties of each object are presented in Table 4. Columns (2) thru (4) list the EWs of the [O III] λ 5007, $H\beta$ and *relative* Fe II emission. Based on studies of broad line asymmetries (see for instance Corbin 1995), we may have systematically overestimated the strength of the [O III] λ 5007 line by using a *symmetric* $H\beta$ line profile component; however, the low S/N and resolution of our spectra did not justify the use of more complicated model line profiles. The FWHM of the forbidden [O III] λ 5007 narrow line is given in column (5). This line width was not tabulated for the three objects (Q1225+317, Q1246-057 and Q1309-056) with no detectable (above noise) [O III] λ 5007 emission. Column (6) lists the total FWHM of $H\beta$, while column (7) gives the FWHM of the broad component of the $H\beta$ line. All three line widths are the intrinsic widths with the instrumental resolution (550 km s^{-1}) removed. Columns (8) and (9) give

the ratios of the EWs of [O III] λ 5007 and Fe II to that of H β . Column (10) lists the ratio of the peak flux of the [O III] λ 5007 line to that of the H β line, the quantity “Peak λ 5007” from BG92. Peak λ 5007 is not as quantitative as EWs or line ratios, but we include it to compare with the low redshift data. QSO 1148-001 has only [O III] λ 5007 EW and FWHM measurements since the H β line fell outside of the spectral coverage of the detector.

To establish the confidence of the emission line property measurements, a Monte Carlo analysis was performed to calculate the errors associated with all quantities tabulated in Table 4 except for those in column (7). The error affiliated with H β _{broad} FWHM was derived from the estimated covariance matrix in the Levenberg-Marquardt fitting routine and was about 8% on average. For the remaining eight properties, the best fit model spectrum of each object was used to create $n = 250$ synthetic spectra. We added random Poisson noise, at a gain of unity, to each normalized composite model in order to produce an artificial spectrum with similar S/N as found in the original data. Then each synthetic spectrum was fitted with our fitting routine, the optimal fit reduced chi-squared χ^2_{ν} was found, and the emission line properties $p_i(n)$ (such that $i =$ emission line property type) were calculated. For each synthetic spectrum, the eight parameters plus the χ^2_{ν} were tabulated in separate Monte Carlo distributions. Each distribution was sorted and the central 68% of its values ($p_i(40)$ to $p_i(210)$) were determined. We assumed that the most likely value of each distribution roughly corresponded to the measured result ($p_i(result)$) tabulated in Table 4. Therefore, the left (–) and right (+) sigmas for each emission line property were found by:

$$\sigma_i(-) = p_i(result) - p_i(40) \tag{8}$$

and

$$\sigma_i(+) = p_i(210) - p_i(result). \tag{9}$$

Figure 3 gives a representative example of the nine Monte Carlo distributions, for PG1247+267. A solid dot representing the parameter’s measured value is plotted above each distribution, as are its left and right sigmas. The uncertainties associated with each of the eight emission line properties are tabulated along with the measured result in Table 4. In general, the Monte Carlo distributions were approximately Gaussian, and on average the mean 1σ for each property was roughly 23% of its measured value.

Table 4. Measured Emission Line Properties

QSO	Equivalent Widths			FWHM			[O III]/H β	Fe II/H β	Peak λ 5007
	λ 5007 (\AA)	H β (\AA)	Fe II ^a (\AA)	λ 5007 (km s ⁻¹)	H β _{total} ^b (km s ⁻¹)	H β _{broad} (km s ⁻¹)			
Q0043+008	16.0 ^{+2.4} _{-1.9}	108.9 ^{+4.8} _{-11.5}	28.9 ^{+4.3} _{-7.3}	910 ⁺¹⁹⁰ ₋₃₀₀	4330 ⁺⁴⁵⁰ ₋₆₆₀	9950 ⁺⁵⁶⁰ ₋₅₆₀	0.15 ^{+0.03} _{-0.02}	0.27 ^{+0.04} _{-0.05}	0.66 ^{+0.11} _{-0.07}
Q0049+007	4.0 ^{+3.4} _{-1.1}	94.6 ^{+5.6} _{-13.3}	64.4 ^{+5.1} _{-12.2}	480 ⁺⁴⁷⁰ ₋₂₁₀	4160 ⁺¹⁰⁴⁰ ₋₁₇₂₀	13440 ⁺¹⁰⁴⁰ ₋₁₀₄₀	0.04 ^{+0.04} _{-0.01}	0.68 ^{+0.06} _{-0.08}	0.48 ^{+0.14} _{-0.13}
Q0049+014	5.0 ^{+1.3} _{-0.7}	55.4 ^{+4.8} _{-5.6}	18.9 ^{+5.0} _{-5.3}	570 ⁺²⁷⁰ ₋₂₈₀	5890 ⁺⁹⁶⁰ ₋₁₄₁₀	13660 ⁺⁹⁵⁰ ₋₉₅₀	0.09 ^{+0.03} _{-0.01}	0.34 ^{+0.07} _{-0.08}	0.69 ^{+0.17} _{-0.15}
Q0109+022	26.2 ^{+3.0} _{-1.5}	32.5 ^{+6.4} _{-4.6}	16.7 ^{+5.5} _{-5.2}	1390 ⁺⁶⁰ ₋₂₀₀	7020 ⁺⁹⁴⁰ ₋₂₁₂₀	9560 ⁺¹¹⁸⁰ ₋₁₁₈₀	0.81 ^{+0.17} _{-0.14}	0.51 ^{+0.11} _{-0.15}	4.52 ^{+0.36} _{-0.96}
Q0123+257	28.1 ^{+4.4} _{-2.3}	55.5 ^{+8.3} _{-9.0}	21.5 ^{+7.2} _{-8.0}	440 ⁺¹⁶⁰ ₋₁₁₀	1160 ⁺³⁸⁰ ₋₃₉₀	5020 ⁺⁵⁸⁰ ₋₅₈₀	0.51 ^{+0.12} _{-0.08}	0.39 ^{+0.10} _{-0.13}	1.34 ^{+0.21} _{-0.18}
Q0153+744	19.5 ^{+1.5} _{-1.5}	74.4 ^{+5.7} _{-5.1}	17.8 ^{+4.0} _{-3.8}	1190 ⁺¹⁹⁰ ₋₂₂₀	5650 ⁺⁴¹⁰ ₋₆₉₀	11470 ⁺⁵⁷⁰ ₋₅₇₀	0.26 ^{+0.03} _{-0.03}	0.24 ^{+0.04} _{-0.04}	1.14 ^{+0.09} _{-0.12}
Q0226-104	2.3 ^{+1.4} _{-0.8}	77.9 ^{+6.3} _{-4.9}	40.8 ^{+6.5} _{-5.8}	1670 ⁺⁴¹⁰ ₋₇₈₀	5490 ⁺⁴⁵⁰ ₋₉₅₀	12850 ⁺⁶⁶⁰ ₋₆₆₀	0.03 ^{+0.02} _{-0.01}	0.52 ^{+0.06} _{-0.06}	0.25 ^{+0.08} _{-0.05}
Q0226-038	31.9 ^{+4.4} _{-2.3}	58.3 ^{+19.9} _{-8.2}	20.1 ^{+9.2} _{-6.9}	1120 ⁺²²⁰ ₋₂₉₀	2780 ⁺⁸⁴⁰ ₋₁₁₃₀	9130 ⁺¹¹⁸⁰ ₋₁₁₈₀	0.55 ^{+0.10} _{-0.12}	0.34 ^{+0.11} _{-0.12}	1.66 ^{+0.21} _{-0.36}
Q0421+019	51.1 ^{+2.3} _{-2.0}	130.3 ^{+7.9} _{-11.3}	31.6 ^{+4.3} _{-5.4}	1370 ⁺¹⁹⁰ ₋₁₉₀	4660 ⁺⁷¹⁰ ₋₈₀₀	14310 ⁺⁶⁵⁰ ₋₆₅₀	0.39 ^{+0.03} _{-0.02}	0.24 ^{+0.03} _{-0.03}	1.49 ^{+0.14} _{-0.12}
Q0424-131	29.8 ^{+2.3} _{-1.6}	80.3 ^{+11.3} _{-3.2}	9.9 ^{+4.4} _{-4.0}	1190 ⁺⁹⁰ ₋₁₉₀	4380 ⁺⁵¹⁰ ₋₆₀₀	9560 ⁺⁵⁷⁰ ₋₅₇₀	0.37 ^{+0.03} _{-0.06}	0.12 ^{+0.04} _{-0.05}	1.44 ^{+0.16} _{-0.14}
Q0552+398	17.2 ^{+2.7} _{-2.1}	35.5 ^{+6.0} _{-4.7}	2.7 ^{+4.1} _{-2.7}	1470 ⁺²³⁰ ₋₃₈₀	2730 ⁺¹⁵⁰ ₋₅₄₀	4700 ⁺⁵⁷⁰ ₋₅₇₀	0.48 ^{+0.09} _{-0.08}	0.07 ^{+0.10} _{-0.07}	0.94 ^{+0.15} _{-0.16}
Q0836+710	1.1 ^{+1.1} _{-0.6}	40.2 ^{+3.3} _{-4.4}	28.2 ^{+3.4} _{-3.9}	1270 ⁺¹⁹⁰ ₋₆₂₀	3410 ⁺¹⁰⁰⁰ ₋₉₃₀	13070 ⁺¹⁰⁰⁰ ₋₁₀₀₀	0.03 ^{+0.04} _{-0.01}	0.70 ^{+0.07} _{-0.07}	0.42 ^{+0.14} _{-0.09}
Q0842+345	6.4 ^{+1.5} _{-1.3}	56.6 ^{+3.7} _{-5.7}	48.6 ^{+5.3} _{-5.8}	1270 ⁺⁸⁸⁰ ₋₅₂₀	8540 ⁺⁶²⁰ ₋₂₅₉₀	15350 ⁺¹⁴⁴⁰ ₋₁₄₄₀	0.11 ^{+0.03} _{-0.02}	0.86 ^{+0.10} _{-0.07}	0.55 ^{+0.14} _{-0.14}
Q1011+091	6.2 ^{+3.0} _{-1.2}	90.3 ^{+13.4} _{-13.6}	77.1 ^{+16.7} _{-15.4}	930 ⁺⁴⁰⁰ ₋₅₂₀	7510 ⁺¹⁴⁶⁰ ₋₂₈₀₀	13500 ⁺¹¹⁹⁰ ₋₁₁₉₀	0.07 ^{+0.04} _{-0.01}	0.85 ^{+0.09} _{-0.10}	0.47 ^{+0.24} _{-0.14}
Q1104-181	14.9 ^{+3.1} _{-1.6}	89.6 ^{+10.0} _{-8.5}	25.7 ^{+7.3} _{-9.3}	1420 ⁺²⁸⁰ ₋₄₁₀	3950 ⁺⁴⁶⁰ ₋₆₆₀	10490 ⁺⁷²⁰ ₋₇₂₀	0.17 ^{+0.05} _{-0.02}	0.29 ^{+0.07} _{-0.09}	0.55 ^{+0.12} _{-0.09}
Q1148-001	22.9 ^{+2.9} _{-0.9}	760 ⁺¹⁴⁰ ₋₁₁₀
Q1158-187	16.3 ^{+5.4} _{-1.5}	82.7 ^{+25.1} _{-11.6}	16.9 ^{+13.8} _{-8.8}	2370 ⁺⁹⁰ ₋₂₈₀	3710 ⁺¹⁰²⁰ ₋₁₁₆₀	15280 ⁺¹⁰⁸⁰ ₋₁₀₈₀	0.20 ^{+0.09} _{-0.06}	0.20 ^{+0.13} _{-0.14}	0.59 ^{+0.27} _{-0.20}
Q1222+228	10.8 ^{+2.8} _{-3.1}	83.1 ^{+8.3} _{-10.5}	31.1 ^{+4.6} _{-6.1}	1040 ⁺¹⁵⁰ ₋₅₄₀	7060 ⁺¹⁷⁴⁰ ₋₁₄₇₀	13650 ⁺⁷⁵⁰ ₋₇₅₀	0.13 ^{+0.04} _{-0.04}	0.37 ^{+0.04} _{-0.07}	0.65 ^{+0.15} _{-0.08}
Q1225+317	0.6 ^{+0.5} _{-0.2}	42.3 ^{+2.9} _{-2.8}	46.8 ^{+3.6} _{-3.3}	...	8300 ⁺⁴²⁰ ₋₁₀₆₀	13420 ⁺⁶⁶⁰ ₋₆₆₀	0.01 ^{+0.01} _{-0.01}	1.11 ^{+0.05} _{-0.05}	0.21 ^{+0.09} _{-0.09}
Q1228+077	9.7 ^{+1.5} _{-1.5}	46.4 ^{+8.0} _{-8.6}	4.1 ^{+5.3} _{-4.5}	960 ⁺⁴¹⁰ ₋₃₂₀	4030 ⁺¹²¹⁰ ₋₉₇₀	5780 ⁺⁷³⁰ ₋₇₃₀	0.21 ^{+0.02} _{-0.01}	0.09 ^{+0.04} _{-0.04}	0.78 ^{+0.13} _{-0.08}
Q1246-057	3.0 ^{+0.7} _{-0.7}	59.6 ^{+2.4} _{-3.1}	47.1 ^{+2.4} _{-2.5}	...	5870 ⁺¹¹³⁰ ₋₆₈₀	14820 ⁺⁵⁴⁰ ₋₅₄₀	0.05 ^{+0.01} _{-0.01}	0.79 ^{+0.03} _{-0.03}	0.14 ^{+0.07} _{-0.02}
Q1247+267	10.4 ^{+3.1} _{-1.3}	77.6 ^{+11.7} _{-0.9}	31.4 ^{+7.5} _{-4.1}	940 ⁺²⁴⁰ ₋₄₃₀	4210 ⁺⁴⁵⁰ ₋₁₀₁₀	7460 ⁺²²⁰ ₋₂₂₀	0.13 ^{+0.05} _{-0.05}	0.40 ^{+0.12} _{-0.09}	0.56 ^{+0.17} _{-0.20}
Q1309-056	2.1 ^{+1.3} _{-0.2}	55.6 ^{+4.2} _{-4.7}	51.2 ^{+3.8} _{-4.3}	...	3220 ⁺⁵⁴⁰ ₋₆₀₀	9620 ⁺⁵⁷⁰ ₋₅₇₀	0.04 ^{+0.03} _{-0.00}	0.92 ^{+0.07} _{-0.06}	0.16 ^{+0.09} _{-0.05}
Q1331+170	18.6 ^{+1.2} _{-0.9}	67.8 ^{+6.9} _{-5.7}	19.1 ^{+3.3} _{-3.3}	1770 ⁺²⁹⁰ ₋₂₆₀	7480 ⁺²⁴⁰ ₋₃₈₀	14550 ⁺⁸⁴⁰ ₋₈₄₀	0.28 ^{+0.02} _{-0.02}	0.28 ^{+0.03} _{-0.03}	1.14 ^{+0.06} _{-0.06}
Q1346-036	2.8 ^{+1.5} _{-0.9}	72.7 ^{+5.6} _{-6.2}	51.3 ^{+3.2} _{-4.1}	370 ⁺⁴¹⁰ ₋₃₇₀	3470 ⁺⁷⁶⁰ ₋₁₆₅₀	10250 ⁺³⁸⁰ ₋₃₈₀	0.04 ^{+0.03} _{-0.02}	0.70 ^{+0.05} _{-0.06}	0.37 ^{+0.10} _{-0.20}
Q1416+091	6.1 ^{+1.1} _{-0.9}	60.8 ^{+3.3} _{-4.3}	11.3 ^{+2.4} _{-5.4}	1740 ⁺³¹⁰ ₋₆₀	4610 ⁺⁴⁶⁰ ₋₅₂₀	10900 ⁺¹⁵⁸⁰ ₋₁₅₈₀	0.10 ^{+0.02} _{-0.01}	0.19 ^{+0.02} _{-0.05}	0.31 ^{+0.05} _{-0.07}
Q1435+638	15.2 ^{+2.1} _{-1.5}	77.4 ^{+10.7} _{-9.4}	26.8 ^{+6.9} _{-6.1}	1020 ⁺²⁹⁰ ₋₇₉₀	6280 ⁺⁵⁵⁰ ₋₉₇₀	11650 ⁺⁹⁰⁰ ₋₉₀₀	0.20 ^{+0.04} _{-0.03}	0.35 ^{+0.09} _{-0.09}	0.96 ^{+0.11} _{-0.07}
Q1448-232	19.9 ^{+2.1} _{-2.1}	78.5 ^{+14.1} _{-9.2}	20.8 ^{+7.5} _{-6.2}	1670 ⁺³⁰⁰ ₋₃₅₀	3230 ⁺⁵⁵⁰ ₋₁₂₈₀	7770 ⁺³⁸⁰ ₋₃₈₀	0.25 ^{+0.04} _{-0.04}	0.26 ^{+0.07} _{-0.06}	0.59 ^{+0.10} _{-0.18}
Q1704+710	19.7 ^{+1.9} _{-1.0}	95.7 ^{+5.1} _{-6.2}	10.6 ^{+3.6} _{-4.0}	940 ⁺⁹⁰ ₋₂₆₀	1560 ⁺²²⁰ ₋₃₇₀	10200 ⁺¹¹⁰⁰ ₋₁₁₀₀	0.21 ^{+0.04} _{-0.02}	0.11 ^{+0.03} _{-0.04}	0.68 ^{+0.08} _{-0.06}
Q2212-179	20.5 ^{+5.5} _{-2.2}	51.5 ^{+21.5} _{-17.7}	13.3 ^{+15.2} _{-10.5}	1200 ⁺³⁷⁰ ₋₂₉₀	6150 ⁺⁴⁹⁰ ₋₆₀₀	11160 ⁺¹⁰²⁰ ₋₁₀₂₀	0.40 ^{+0.07} _{-0.03}	0.26 ^{+0.12} _{-0.11}	1.83 ^{+0.14} _{-0.12}
Q2251+244	14.7 ^{+1.8} _{-1.4}	28.0 ^{+3.7} _{-6.0}	34.3 ^{+2.2} _{-4.2}	840 ⁺²⁴⁰ ₋₃₀₀	4910 ⁺²⁹⁰ ₋₁₅₉₀	9190 ⁺⁹⁷⁰ ₋₉₇₀	0.53 ^{+0.07} _{-0.04}	1.23 ^{+0.05} _{-0.08}	2.65 ^{+0.28} _{-0.30}
Q2310+385	28.7 ^{+1.3} _{-1.7}	92.2 ^{+4.9} _{-3.3}	75.2 ^{+5.3} _{-3.3}	1130 ⁺¹⁴⁰ ₋₁₇₀	3050 ⁺⁸⁵⁰ ₋₁₄₆₀	8520 ⁺⁸¹⁰ ₋₈₁₀	0.31 ^{+0.08} _{-0.12}	0.82 ^{+0.14} _{-0.14}	1.17 ^{+0.41} _{-0.45}

^aRelative EW measured over 4810 – 5090 \AA .

^bTotal (narrow + broad) FWHM.

4. Correlation Analysis

Having measured and tabulated a host of continuum and emission line properties for this QSO sample, we proceeded to explore whether the various parameters correlate with one another. To this end, we calculated the Spearman rank-order correlation matrix, along with its significance matrix, for the following set of properties: (i) the apparent V magnitude and systemic redshift from Table 1; (ii) the five continuum parameters from Table 2; (iii) the nine rest-frame optical measurements from Table 4; and (iv) the rest-frame UV emission FWHMs and EWs compiled from the literature and tabulated in Tables 5 and 6, respectively. The complete correlation coefficient matrix is shown in Table 7. The correlation coefficients r_s were computed using only those objects that had both involved values tabulated. In addition to the Spearman statistic, we calculated the Kendall nonparametric (τ) correlation coefficient and confidence matrices.

For our total sample size of $N = 32$ objects, a significant correlation at the $\gtrsim 95\%$ confidence level corresponds to a coefficient of $|r_s| \gtrsim 0.35$, with a negative coefficient indicating an anti-correlation. This 95% significance was derived from the two-sided probability ($= 0.05$) of getting the *same* coefficient from an uncorrelated sample. Measures of more significant correlations for the same sample size are $|r_s| \gtrsim 0.47$ (for $\gtrsim 99\%$) and $|r_s| \gtrsim 0.57$ (for $\gtrsim 99.9\%$). A set of 22 different properties results in $22 \times \frac{21}{2} = 231$ correlation coefficients; therefore, we would expect $\lesssim 3$ spurious events at 99% confidence. For the Spearman analysis, we find 34 correlations (both positive and negative) significant at the $\geq 99\%$ level: 9 are due to correlations between *dependent* parameters; 10 are *degenerate* correlations; and therefore, 15 are *independent* correlations at the $\geq 99\%$ level. The highly correlated ($r_s = +0.82$) V and H apparent magnitudes is an example of a dependent correlation since H was calculated directly from V for most of the sample. A correlation is degenerate when multiple parameters have been used to quantify a single property (*e.g.* [O III] λ 5007 EW, [O III]/H β ratio and Peak λ 5007 are all measures of [O III] λ 5007 emission strength), and these parameters *all* correlate with another property, such as $\log(R')$. The 15 independent correlations, as well as other less significant independent relations confirmed in lower redshift/luminosity studies, are tabulated in Table 8. The number of correlated pairs, plus the computed coefficients and corresponding confidence levels for both the Spearman and Kendall statistics, as well as the number of degenerate (at $\geq 95\%$ confidence) correlations are all presented for each result. The relevance and interpretation of the majority of these findings are discussed in detail below.

Table 5. Rest-frame Ultraviolet Emission Line Widths

QSO	C IV $\lambda 1549$ (km s ⁻¹)	Refs. ^a	C III] $\lambda 1909$ (km s ⁻¹)	Refs. ^a
Q0043+008	3000	1	4450	1,2
Q0049+007	8300	3 ^b	7400	4
Q0049+014	8200	3 ^b	10810	5
Q0109+022	5260	5	8120	5
Q0123+257	4700	1	3600	1
Q0153+744	5250	6	5630	6
Q0226-104	6772	7 ^c	9014	7
Q0226-038	4500	1,4,8,9	6750	1,4
Q0421+019	5100	10	5380	4,8
Q0424-131	2820	4,9	4650	1,4
Q0552+398	3000	3 ^b
Q0836+710	6740	6	11200	6,11
Q0842+345	6800	12 ^b
Q1011+091	10000	1	11000	1,2
Q1104-181	6400	13 ^b	9900	13 ^b
Q1148-001	2740	1,4,9	4100	4
Q1158-187	4045	14
Q1222+228	4840	1,9,15 ^b	6000	1
Q1225+317	10350	1,16	12300	1,16
Q1228+077	4000	1
Q1246-057	5000	1	9200	1,2,4
Q1247+267	3610	1,9,15 ^b	5500	1,10
Q1309-056	5000	1	11300	1,2,7
Q1331+170	5210	1,9,16	6500	1,16,17
Q1346-036	10000	1	11680	14
Q1416+091	7500	4
Q1435+638	4200	4,9	4242	4,18
Q1448-232	3610	14	4105	14
Q1704+710	6000	4
Q2212-179	3000	1
Q2251+244	6600	19	8700	19
Q2310+385	4300	20 ^b

^aMultiple references indicate that the value is an average.

^bThe line width was measured directly off the published spectrum.

^cFWHM derived from red HWHM.

References. — (1) Turnshek 1984; (2) Hartig & Baldwin 1986; (3) Wolfe *et al.* 1986; (4) Brotherton *et al.* 1994a; (5) Schneider *et al.* 1994; (6) Lawrence *et al.* 1996; (7) WMFH91; (8) Tytler & Fan 1992; (9) Wills *et al.* 1993; (10) Baldwin *et al.* 1989; (11) Stickel & Kühr 1993; (12) Thompson *et al.* 1989; (13) Wisotzki *et al.* 1993; (14) Ulrich 1989; (15) Sargent *et al.* 1988; (16) Corbin 1992; (17) Carswell *et al.* 1991; (18) Laor *et al.* 1995; (19) Corbin 1991; (20) Wills 1997.

Table 6. Rest-frame Ultraviolet Emission Line Equivalent Widths

QSO	Ly α λ 1216 (\AA)	Refs. ^a	C IV λ 1549 (\AA)	Refs. ^a	C III] λ 1909 (\AA)	Refs. ^a	Mg II λ 2798 (\AA)	Refs. ^a
Q0043+008	98.7	1	7.0	1,2 ^b	15.0	2,3	52.0	3
Q0049+007	100.0	4 ^c	29.0	4 ^c	20.7	5
Q0049+014	92.0	4 ^c	20.0	6,4 ^c	17.0	6
Q0109+022	24.0	6	18.0	6
Q0123+257	83.0	4 ^c
Q0153+744	48.7	7	38.0	7	26.3	7	17.2	7
Q0226-104	14.8	2 ^b	24.6	2
Q0226-038	56.2	1,8	26.7	1,5,8,9	13.5	5,8	30.4	5
Q0421+019	42.2	1,8	16.6	1,8	15.2	5	27.5	5
Q0424-131	84.8	1	39.4	1,5,9	19.5	5	18.2	5
Q0552+398	6.0	4 ^c
Q0836+710	10.5	10	20.1	10
Q0842+345	15.0	11 ^c
Q1011+091	15.8	2 ^b	12.0	2,3	18.0	3
Q1104-181	10.4	12	15.7	12
Q1148-001	112.0	8	27.4	5,8,9	10.4	5,8	31.1	5
Q1158-187	31.0	13
Q1222+228	78.0	8	25.7	8,9
Q1225+317	6.9	14
Q1228+077
Q1246-057	9.6	2 ^b	17.9	2,3,5	29.0	3
Q1247+267	86.5	8	29.8	8,9	19.7	8
Q1309-056	16.2	2 ^b	18.4	2,3	20.0	3
Q1331+170	63.0	14	23.9	15,14,9	25.0	15,14	16.0	15
Q1346-036	140.0	4 ^c	32.3	4,13	16.7	13
Q1416+091	18.2	5	28.2	5
Q1435+638	83.3	14	34.0	5,14,9	10.1	5,14,16	21.6	5,16
Q1448-232	105.0	14	21.2	14,13	16.7	14,13
Q1704+710	18.7	5	27.3	5
Q2212-179
Q2251+244	6.0	17	5.0	17	22.0	17
Q2310+385	110.0	18 ^c	38.0	18 ^c

^aMultiple references indicate that the value is an average.

^bFull EW derived from red half of emission line.

^cThe line width was measured directly off the published spectrum.

References. — (1) Osmer *et al.* 1994; (2) WMFH91; (3) Hartig & Baldwin 1986; (4) Wolfe *et al.* 1986; (5) Steidel & Sargent 1991; (6) Schneider *et al.* 1994; (7) Lawrence *et al.* 1996; (8) Baldwin *et al.* 1989; (9) Wills *et al.* 1993; (10) Stickel & Kühr 1993; (11) Thompson *et al.* 1989; (12) Wisotzki *et al.* 1993; (13) Ulrich 1989; (14) Corbin 1992; (15) Carswell *et al.* 1991; (16) Laor *et al.* 1995; (17) Corbin 1991; (18) Wills 1997.

TABLE 7
SPEARMAN RANK-ORDER CORRELATION COEFFICIENT MATRIX

Property	(1)	(2)	(3)	(4)	(5)	(6)	(7)	(8)	(9)	(10)	(11)	(12)	(13)	(14)	(15)	(16)	(17)	(18)	(19)	(20)	(21)	(22)
(1) $H\beta_{\text{pond}}$ FWHM	...	+0.30	+0.21	+0.63	-0.35	+0.20	-0.48	-0.35	-0.29	-0.36	-0.15	+0.38	-0.35	+0.22	+0.50	+0.35	-0.24	-0.10	+0.03	-0.25	-0.42	+0.60
(2) Fe II EW	+0.30	...	+0.25	+0.18	-0.47	+0.85	-0.52	-0.10	-0.25	-0.03	-0.07	+0.08	-0.45	-0.35	+0.56	+0.45	+0.30	-0.15	-0.13	+0.13	-0.38	+0.48
(3) $H\beta$ EW	+0.21	+0.25	...	-0.10	-0.11	-0.20	-0.12	-0.16	-0.19	-0.11	-0.40	+0.05	+0.23	-0.05	-0.10	-0.42	+0.29	+0.34	-0.25	+0.01	-0.47	+0.59
(4) $H\beta_{\text{ratio}}$ FWHM	+0.63	+0.18	-0.10	...	-0.05	+0.27	-0.20	-0.22	-0.27	-0.42	-0.12	+0.48	-0.24	+0.10	+0.38	+0.20	-0.42	-0.12	+0.03	-0.50	-0.28	+0.48
(5) Peak λ 5007	-0.35	-0.47	-0.11	-0.05	...	-0.36	+0.92	+0.33	+0.53	+0.19	+0.05	-0.19	+0.84	-0.06	-0.43	-0.57	-0.71	+0.32	-0.03	-0.13	+0.31	-0.40
(6) Fe II ratio ^a	+0.20	+0.85	-0.20	+0.27	-0.36	...	-0.43	-0.06	-0.21	-0.03	+0.07	+0.09	-0.51	-0.37	+0.64	+0.64	+0.24	-0.29	+0.01	-0.02	-0.16	+0.19
(7) [O III] ratio ^a	-0.48	-0.54	-0.16	-0.25	+0.93	-0.43	...	+0.33	+0.58	+0.23	+0.11	-0.25	+0.90	+0.17	-0.51	-0.92	-0.62	+0.23	+0.02	-0.06	+0.46	-0.56
(8) V	-0.35	-0.10	-0.16	-0.22	+0.33	-0.06	+0.26	...	+0.06	+0.82	+0.35	-0.75	+0.23	-0.25	-0.08	+0.06	+0.22	-0.10	+0.01	+0.01	-0.02	-0.39
(9) $\log(R')$	-0.29	-0.25	-0.19	-0.27	+0.53	-0.21	+0.51	+0.06	...	+0.22	-0.08	-0.29	+0.48	-0.09	-0.28	-0.46	-0.32	+0.04	-0.05	+0.16	+0.57	-0.55
(10) H	-0.36	-0.03	-0.11	-0.42	+0.19	-0.03	+0.27	+0.82	+0.22	...	+0.30	-0.96	+0.15	-0.37	-0.11	+0.01	+0.18	-0.11	+0.04	+0.15	-0.09	-0.34
(11) τ_{sys}	-0.15	-0.07	-0.40	-0.12	+0.65	+0.07	+0.09	+0.35	-0.08	+0.30	...	-0.06	-0.18	-0.03	+0.27	+0.40	+0.04	-0.21	+0.23	-0.48	+0.11	-0.30
(12) $\log(L_{\nu}(V))$	+0.38	+0.08	+0.05	+0.48	-0.19	+0.09	-0.30	-0.75	-0.29	-0.96	-0.06	...	-0.25	+0.29	+0.24	+0.09	-0.16	+0.08	+0.01	-0.33	+0.07	+0.36
(13) [O III] EW	-0.36	-0.43	+0.22	-0.25	+0.86	-0.47	+0.90	+0.27	+0.48	+0.17	-0.14	-0.26	...	+0.10	-0.55	-0.74	-0.31	+0.44	-0.20	+0.12	+0.29	-0.37
(14) [O III] FWHM	+0.22	-0.35	-0.05	+0.10	-0.06	-0.37	+0.13	-0.25	-0.09	-0.37	-0.03	+0.29	+0.13	...	-0.15	+0.05	-0.38	-0.18	+0.25	-0.48	+0.18	-0.04
(15) C IV FWHM	+0.50	+0.56	-0.10	+0.38	-0.43	+0.64	-0.53	-0.08	-0.28	-0.11	+0.27	+0.24	-0.60	-0.15	...	+0.81	-0.23	-0.28	+0.29	-0.67	-0.17	+0.22
(16) C III FWHM	+0.35	+0.45	-0.42	+0.29	-0.57	+0.64	-0.64	+0.06	-0.46	+0.01	+0.40	+0.09	-0.76	+0.05	+0.81	...	-0.13	-0.45	+0.19	-0.27	-0.12	+0.01
(17) Ly α EW	-0.24	+0.30	+0.29	-0.42	-0.71	+0.24	-0.63	+0.22	-0.32	+0.18	+0.04	-0.16	-0.29	-0.38	-0.23	-0.13	...	+0.28	-0.31	+0.45	-0.34	+0.11
(18) C IV EW	-0.10	-0.15	+0.34	-0.12	+0.32	-0.29	+0.23	-0.10	+0.04	-0.11	-0.21	+0.08	+0.41	-0.18	-0.28	-0.45	+0.28	...	+0.01	-0.35	-0.24	+0.23
(19) C III EW	+0.03	-0.13	-0.25	+0.03	-0.03	+0.01	+0.09	+0.01	-0.05	+0.04	+0.23	+0.01	-0.29	+0.25	+0.29	+0.19	-0.31	+0.01	...	-0.56	-0.14	+0.21
(20) Mg II EW	-0.25	+0.13	+0.01	-0.50	-0.13	-0.02	-0.05	+0.01	+0.16	+0.15	-0.48	-0.33	+0.12	-0.48	-0.67	-0.27	+0.45	-0.35	-0.56	...	+0.00	-0.02
(21) $\log(L_{\nu}(2\text{keV}))$	-0.42	-0.38	-0.47	-0.28	+0.31	-0.16	+0.35	-0.02	+0.57	-0.09	+0.11	+0.07	+0.25	+0.18	-0.17	-0.12	-0.34	-0.24	-0.14	+0.00	...	-0.84
(22) α_{rel}	+0.60	+0.48	+0.59	+0.48	-0.40	+0.19	-0.45	-0.39	-0.55	-0.34	-0.30	+0.36	-0.32	-0.04	+0.22	+0.01	+0.11	+0.23	+0.21	-0.02	-0.84	...

^aRatio to $H\beta$ EW.

Table 8. Significant Correlations

Correlated Properties	N_{pairs}	r_s	Spearman		τ	Kendall	
			CL ^a	$N_{\text{deg}}^{\text{b}}$		CL ^a	$N_{\text{deg}}^{\text{b}}$
[O III] strength - Fe II strength	31	-0.524	99.8	5	-0.366	99.6	5
[O III] strength - $\log(R')$	31	+0.508	99.6	2	+0.421	99.9	2
[O III] strength - C III] FWHM	26	-0.762	> 99.9	2	-0.561	> 99.9	2
[O III] strength - C IV FWHM	30	-0.599	> 99.9	2	-0.433	99.9	2
[O III] strength - $H\beta_{\text{broad}}$ FWHM	31	-0.478	99.4	1	-0.297	98.1	1
[O III] strength - α_{ox}	24	-0.455	97.4	1	-0.312	96.7	2
[O III] EW - C IV EW ^c	27	+0.415	96.9	0	+0.280	95.9	0
[O III] strength - Ly α EW	16	-0.629	99.1	1	-0.467	98.8	1
$H\beta$ FWHM - Luminosity	31	+0.482	99.4	4	+0.326	99.0	4
$H\beta$ FWHM - α_{ox}	24	+0.598	99.8	2	+0.449	99.8	2
$H\beta$ FWHM - C IV FWHM	29	+0.499	99.4	1	+0.328	98.7	0
$H\beta$ EW - α_{ox}	24	+0.590	99.8	1	+0.428	99.7	1
$H\beta$ EW - Redshift ^d	31	-0.401	97.5	0	-0.284	97.5	0
Fe II EW - α_{ox}	24	+0.481	98.3	0	+0.319	97.1	0
Fe II strength - C IV FWHM	29	+0.645	> 99.9	1	+0.476	> 99.9	1
Fe II strength - C III] FWHM	25	+0.645	99.9	1	+0.457	99.9	1
C IV FWHM - C III] FWHM	24	+0.808	> 99.9	0	+0.630	> 99.9	0
$\log(R')$ - α_{ox}	25	-0.547	99.5	1	-0.380	99.2	1

^aConfidence Level

^bNumber of additional “like” (degenerate) correlations, significant at $\geq 95\%$ confidence.

^cConfirmed at lower redshift by Corbin & Boroson (1996).

^dConfirmed in $z \lesssim 1$, RLQ only sample (Brotherton 1996).

4.1. Correlations with the Strength of [O III] λ 5007 Emission

We find that all measures of [O III] emission strength are anti-correlated, at $> 95\%$ confidence, with the optical Fe II emission strength. The most significant example is [O III]/ $H\beta$ to Fe II EW (99.8% confidence), which is plotted in Figure 4a. This anti-correlation was the most significant one found by BG92, and at lower redshift by Corbin & Boroson (1996). It was also seen by Brotherton (1996) in an entirely RLQ sample at $z \leq 0.95$. As an explanation, BG92 and Wills & Brotherton (1996) have proposed that a large covering fraction by dense, high-speed Fe II-rich clouds will result in high Fe II emission and at the same time will prevent much of the ionizing radiation from reaching the more distant, low density NLR gas where the forbidden [O III] emission originates. BG92 suggested that this BELR covering factor is dependent on the accretion rate and the mass of the black hole, while Wills (1996) added that greater nuclear obscuration by dust associated with a torus could result in stronger Fe II emission. Recently, dust has been detected in a handful of high redshift QSOs (Cimatti *et al.* 1998).

We also find $> 99\%$ confidence level correlations between all measures of [O III] emission and the radio-to-optical flux ratio R' , measuring the degree of radio loudness. The most significant (99.6%) result is the [O III]/ $H\beta$ to $\log(R')$ correlation plotted in Figure 4b. BG92 found similar, but weaker, correlations. It is problematic to explain this relationship in terms of orientation (thus, unification of RLQs and RQQs), since Jackson & Browne (1991) found that the EW of [O III] is anti-correlated with the ratio of core-to-lobe luminosity, which is a strong indicator of the alignment between the radio axis and the line-of-sight in low redshift RLQs. They proposed that near face-on views show a beamed continuum that swamps the NLR emission, thus significantly reducing the [O III] EW. Instead, we propose that the intensity and direction of the radio power produced by the central engine is closely tied to the intensity and direction of the NLR ionizing radiation. Possible physical mechanisms for this intimate association between the NLR ionization and the radio component are radio jet driven radiative shocks (Wilson *et al.* 1993; though this is a very inefficient mechanism Laor 1998), or anisotropic ionization of the NLR by the nuclear continuum photons emitted preferentially along the radio axis (Bower *et al.* 1995, and Simpson *et al.* 1996). An extension of the latter idea is that the nuclear ionizing continuum is collimated by the opening of a dusty torus which is also roughly aligned with the radio axis (Wilson 1997). Supporting this hypothesis are a host of HST observations of local Seyfert galaxies in the light of [O III] λ 5007 (*e.g.* Wilson *et al.* 1993; Bower *et al.* 1995; and Simpson *et al.* 1996), showing sharp edged, V-shaped profiles believed to be the projection of a biconical NLR, and these cones are generally well aligned with the radio axis. In addition, [O III] emission has been found to be partially obscured in low redshift radio loud AGN via polarization (di Serego Alighieri *et al.* 1997) and by the [O III] λ 5007/[O II] λ 3727 ratio (Baker 1997; and Crawford & Vanderriest 1997).

Further, we find that the FWHM of the two rest-frame UV broad lines (C IV λ 1549 and C III] λ 1909) are anti-correlated with several measures of [O III] emission strength. Especially significant, at $> 99.9\%$ confidence, are the relations between [O III] EW and the FWHM of each carbon line: (i) C III] shown in Figure 4c; and (ii) C IV presented in Figure 4d. The former

relation was predicted and then found in a similar $z \sim 2$ sample by Brotherton (*et al.* 1994b, 1997). A weak [O III] EW to C IV FWHM anti-correlation was found by Corbin & Boroson 1996. Brotherton and Wills (Wills *et al.* 1993; Brotherton *et al.* 1994a,b; Wills & Brotherton 1996; etc.) have argued that these UV broad emission line profiles (C IV and C III]) have two components, a narrow ($v_{FWHM} \sim 2000 \text{ km s}^{-1}$) core arising from an intermediate-line-region (ILR), and a very-broad-line-region (VBLR, $v_{FWHM} \gtrsim 7000 \text{ km s}^{-1}$) base. They have proposed that the ILR is an inner extension of the NLR and that this physical connection between the two regions would produce the observed anti-correlation, such that narrow C III] λ 1909 and C IV] λ 1549 lines are the signature of strong ILR emission, combined with large [O III] EW indicative of strong NLR emission.

We also find an anti-correlation between [O III]/H β and broad H β FWHM (at 99.4%) plotted in Figure 4e. However, this inverse relation cannot be explained with the VBLR+ILR model since the strength of NLR emission anti-correlates only with the *broad* component of H β and not with the total line width. If there were an ILR component of the H β emission, one would expect the total line FWHM to decrease while the total line EW increases with larger NLR strength. An [O III] EW – H β FWHM relation was not found in low redshift/luminosity studies (Corbin & Boroson 1996, and Brotherton 1996); and, BG92 suggested they observed only a slight negative trend between their main eigenvector (the [O III] – Fe II anti-correlation) and the width of broad H β .

The impact of the shape and strength of the ionizing continuum on the line emission manifests itself in an anti-correlation (97.4% significance) between the ratio [O III]/H β and the optical-to-X-ray spectral slope α_{ox} (see Figure 4f), also found by BG92 in their low redshift/luminosity sample. This spectral index is a rough measure of the strength of the ionizing continuum emitted from the optical to the soft X-ray, such that $\alpha_{ox} \gtrsim 1.4$ corresponds to a *steeper* slope and thus a *softer* ionizing continuum, whereas, $\alpha_{ox} \lesssim 1.4$ indicates a *flatter* and *harder* ionizing continuum. A flatter slope is thought to contain two components: (i) a harder non-thermal component of emission produced by the inverse Comptonization of the beamed radio jet photons; and (ii) a softer thermal component emitted from the hot inner edges of the accretion disk. Therefore, this anti-correlation supports the hypothesis that the NLR is ionized by the nuclear continuum.

It should be noted that the one obvious outlier seen in Figures 4a, 4b, 4e and 4f is Q0109+022 (UM87). This is a RQQ with anomalously strong [O III] compared to H β , as well as weak Fe II emission, which are both indicative of the RLQ class. The radio flux measurement, though an upper limit based on detection sensitivity, has been confirmed by the recent NRAO VLA Sky Survey (NVSS – Condon *et al.* 1996). Therefore, the placement of this data point at the extreme end of [O III]/H β values is due to the very weak H β emission apparent in the observed spectrum (see Figure 1d), which may be partially due to the low S/N of the data.

4.2. Correlations with the Width of H β Emission

We find a significant (99.4% confidence) correlation between the total fitted H β FWHM and the intrinsic rest-frame V -band luminosity density, $L_\nu(V)$ (see Figure 5a). At lower redshifts ($z < 1$) and luminosities, similar weak relations have been found between H β FWHM and the luminosity of the rest-frame B -band (Wang, Brinkmann & Bergeron 1996), as well as between broad H β FWHM and the absolute V -band magnitude (BG92). However, Corbin & Boroson (1996) did not find this correlation. This observed trend is consistent with BELR clouds in semi-flattened, gravitationally bound orbits about the nucleus as favored by recent reverberation studies (Wang, Zhou & Gao 1996). On average, an increased luminosity will correspond to a larger central black hole mass, thus correlating with a larger orbital velocity.

We find that the broad H β line width and the mean spectral slope α_{ox} are correlated at the 99.8% level (see Figure 5b). This correlation is consistent with a viewing angle effect, if we assume that the BELR clouds orbit and that α_{ox} is a good inclination indicator (Wang, Brinkmann & Bergeron 1996). In a nearly face-on view one would observe a narrower BELR emission line and a flatter (small α_{ox}) ionizing continuum slope, suggesting a direct view of the harder component of X-rays. Wills & Brotherton (1995; as well as Baker & Hunstead 1995) showed that H β FWHM is inversely correlated with another property measuring the beaming angle in low redshift quasars. Jackson & Browne (1991) confirmed that the Balmer line profile narrows systematically with increasing face-on orientation in a RLQ only study. In contrast to the above results, both Wang, Brinkmann & Bergeron (1996) and Laor *et al.* (1997) have found anti-correlations between H β line width and α_{ox} at low redshift/luminosity. In addition, BG92 and Brotherton (1996) found no correlation in their samples. Note that we do not find any correlations between α_{ox} and the other two broad line widths (C III] and C IV), but recall that the width of these rest UV lines may be related to the fractional contribution from the proposed ILR (see Wills and Brotherton references herein).

Lastly, we find that broad H β FWHM and C IV λ 1549 FWHM are correlated at the 99.4% level (see Figure 5c); however, we find the broad component of the H β line to be, on average wider, than the total C IV line. We suggest that the *broad* components of each line are emitted from the same VBLR, but that the C IV line has an additional, narrower component produced in a separate volume of gas, possibly the proposed ILR. Presumably, the ILR component superimposed on the VBLR component would result in a narrower total line width measurement. Similar correlations have been found at low redshift in a RLQ/RQQ sample (Corbin & Boroson 1996) and a RLQ only sample (Marziani *et al.* 1996).

4.3. Correlations with the Strength of H β Emission

In Figure 6 we present the significant (99.8% confidence) positive correlation between the EW of the total fitted H β emission and the slope of the ionizing continuum, estimated by α_{ox} . As with

the $H\beta$ line width to ionizing continuum slope relation, a significant but *opposite* result was found at low redshift/luminosity (BG92 and Wang, Brinkmann & Bergeron 1996), while Brotherton (1996) and Wilkes (*et al.* 1997) found no correlation with α_{ox} .

4.4. Correlations with the Strength of Optical Fe II Emission

In addition to our confirmation of BG92’s strongest result (see §4.1), we find the optical Fe II EW and the optical-to-X-ray spectral slope α_{ox} to be positively correlated at the 98.3% level (see Figure 7a). It has been shown that strong Fe II emission is associated with softer X-ray spectra in PG QSOs (Laor *et al.* 1994) and in narrow line AGN (Boller, Brandt & Fink 1996), yet this correlation was not found in several low redshift/luminosity QSO samples (BG92; Brotherton 1996; Wang, Brinkmann & Bergeron 1996; and Wilkes *et al.* 1997). Furthermore, our finding is not in agreement with photo-ionization models (*e.g.* Kwan & Krolik 1981; and Netzer & Wills 1983) which predict that hard, flat X-ray spectra are expected to produce strong Fe II emission.

We also find that both parameters of optical Fe II emission strength (Fe II EW and Fe II/ $H\beta$) are correlated with the rest-frame UV line widths of C IV λ 1549 and C III] λ 1909 at $> 97.7\%$ confidence. In fact, the Fe II/ $H\beta$ ratio gives correlations with both carbon line widths at $\geq 99.9\%$ significance (see Figures 7b and 7c). A similarly strong Fe II strength – C III] width correlation was found in another $z \sim 2$ sample (Brotherton 1997). Brotherton suggested that this result was another consequence of the [O III] – Fe II anti-correlation which relates QSO properties from the radio to the X-ray such that variations along this relation (BG92’s first eigenvector) may be a “fundamental plane” for QSOs. These strong positive correlations between Fe II emission strength from the VBLR and the widths of the carbon lines from an ILR, combined with the inverse correlations between NLR emission strength and ILR line widths (see §4.1), give credence to the VBLR+ILR model proposed by Brotherton and Wills. A word of caution — the FWHM of C IV (and of C III] when no C IV measurement was available) was used to broaden the Fe II template used to fit this sample of spectra. In addition, the C IV and C III] line widths are extremely well correlated ($r_s = +0.808$; see below). Thus, the Fe II strength, determined by the best-fit model, could have been biased in such a way as to produce, or at least reinforce, the aforementioned positive correlations. Increased broadening of the iron template may have resulted in confusion between the continuum and the very blended Fe II emission, and thus an overestimate of the Fe II strength. However, we do find a strong correlation between the line widths of C IV and $H\beta$ (see §4.2), which is consistent with BG92’s finding that the widths of Fe II and $H\beta$ are similar, and justifies our use of the C IV line width for broadening the Fe II template. In addition, our Monte Carlo analysis did *not* show any particularly large variations in Fe II EW uncertainties, which would have been evidence for confusion between the continuum and Fe II templates.

4.5. Other Significant Correlations

As stated above, we find a very significant ($> 99.99\%$), correlation between the FWHMs of the two UV, high ionization broad carbon lines taken from the literature (C IV and C III]). The same equally strong result has been found at $z \sim 2$ (Corbin 1991) and at low redshift/luminosity (Corbin & Francis 1994; and Brotherton *et al.* 1994a).

And finally, we find that the degree of radio loudness $\log(R')$ is anti-correlated with the slope of the ionizing continuum α_{ox} , at 99.5% significance. This is consistent with a physical connection between the strength of the ionizing continuum and the strength of the radio power, both believed to be produced by the nuclear source.

5. Luminosity or Redshift Dependencies

An important question that can be asked about our correlation analysis of the previous section is whether any of the emission line properties are dependent on luminosity and/or redshift. Though the luminosity of our sample is fairly constant (see Figure 8), and the redshift range $2.0 \leq z \leq 2.5$ only spans a very small portion of the total age of the Universe τ_0 , any relationships between QSO emission parameters and redshift or luminosity could be evidence for evolutionary effects. This might especially be true if we compared QSOs at $z \sim 2.5$, corresponding to a look back time of nearly 80% (for $q_0 = 0.1$) of τ_0 , to QSOs existing in the local Universe. The QSOs of our high redshift sample do not have similarly luminous counterparts in the nearby Universe. Thus, dependencies on redshift and luminosity are entangled. With these points in mind, we attempted to combine the measurements of the rest-frame optical spectral features of our high redshift, high luminosity data with similar measurements from the low redshift ($z \lesssim 0.5$) and lower luminosity sample (see again Figure 8) of BG92. This combined data set enabled us to search for such dependencies using the most luminous QSOs observed at the two ends of the redshift range spanning $0 < z < 2.5$.

5.1. The Low Redshift Sample

To achieve our goal of creating a consistent $0 < z < 2.5$ QSO sample, it was necessary to combine our high redshift measurements with matching parameters from the low redshift sample. Foremost in importance was the need for equivalent luminosity measurements, therefore, we calculated the rest-frame V -band luminosity density (in $\text{ergs s}^{-1} \text{Hz}^{-1}$) of each low redshift QSO:

$$L_\nu(V) = 4\pi(10\text{pc})^2 F_\nu^i(V), \quad (10)$$

where the *intrinsic* V -band flux density (in $\text{ergs cm}^{-2} \text{s}^{-1} \text{Hz}^{-1}$) is

$$F_\nu^i(V) = 10^{-0.4M_V - 22.41}, \quad (11)$$

derived from BG92’s tabulated absolute magnitude (M_V), assuming that zero magnitude in V is 3880 Jy (Johnson 1966). BG92 calculated M_V from the apparent V of Neugebauer *et al.* (1987), assuming an $H_0 = 50 \text{ km s}^{-1} \text{ Mpc}^{-1}$ and $q_0 = 0.1$ cosmology.

Second, we obtained consistent emission line property measurements by running our χ^2 minimization composite model fitting routine on the entire sample of 87 reduced, rest-frame spectra from BG92. We used the same template set as for the fitting of our high redshift sample, except the narrowest [O III] and $H\beta$ templates were set to the instrumental resolution of the BG92 spectra (450 km s^{-1}). As with our sample, we inspected each spectrum, fitting the upper half of the $H\beta$ line with a Gaussian to determine the line center and then shifting the Balmer template set accordingly for each object. We also rebinned each spectrum to a logarithmic dispersion of 3.5 \AA per pixel for compatibility with the fitting routine. The wavelength coverage of the BG92 sample was greater than in ours, resulting in the detection of the $H\gamma\lambda 4340$ line in most of the objects. From initial fitting tests we found that our set of Balmer templates, with a fixed ratio between $H\beta$ and $H\gamma$, usually did not match the actual data, either producing an overestimate or underestimate of the $H\beta$ line flux. Thus it was necessary to trim the blue half of the $H\gamma$ line from each spectrum prior to fitting.

Since these quasars are at low redshifts, the probability of finding a C IV line width in the literature is very small; therefore, we decided to use the $H\beta$ line FWHM of each object to broaden its Fe II template. This decision is consistent with BG92’s finding that the optical Fe II and Balmer hydrogen emission originate from the same clouds in the BELR. However, we decided not to use their published values of the *broad* $H\beta$ FWHM because these did not include the narrow line component of the permitted emission that the *total* line FWHM of our model does, plus there is no evidence that the permitted Fe II emission is solely comprised of a broad line component. Instead we used a first iteration fit of each spectrum with a larger set of templates to obtain the *total* $H\beta$ line width. The larger set of templates included the 3 power-law, 5 [O III] and 5 Balmer templates, plus a set of 8 Fe II templates broadened by Gaussians of 450 (instrumental width), 1370, 1940, 2740, 3870, 5480, 7320 and 10350 km s^{-1} . These line widths were factors of $\frac{1}{\sqrt{2}}$ of the minimum (2740 km s^{-1}) and maximum (10350 km s^{-1}) C IV line widths from our high redshift sample. From the first iteration fit of 21 templates we obtained the *total* $H\beta$ line width, which was used to broaden the single, object-specific, Fe II template for the final (14 template) fitting iteration of each quasar spectrum. The final best fit composite models for the BG92 sample were quite remarkable in their reproduction of most of the spectral features. The fit to the data and the individual components for a representative object (PG1404+226) are plotted in the top and bottom panels, respectively, of Figure 9.

As with our high redshift sample, the set of emission line properties for each QSO were derived directly from the individual components of its composite model spectrum. In Figure 10 we plot our best fit derived values versus the published BG92 results for the EWs of [O III] $\lambda 5007$ and $H\beta$, the *relative* EW of optical Fe II, and the Peak $\lambda 5007$ parameter. In each case the agreement is excellent for the two properties associated with the [O III] $\lambda 5007$ strength. For Fe II EW there

is a trend such that the BG92 value is greater than our model fit value. This trend is due to a difference in *relative* EW definitions: BG92 selected the strong Fe II emission complex between 4434 and 4684 Å; whereas we chose the spectral range encompassing the H β and [O III] λ 5007 lines where there is much less Fe II emission. There is also a slight trend where the BG92 H β EW is, on average, stronger than our fitted value. We believe this trend is due to BG92’s systematic overestimation of the Fe II strength, thereby producing a lower continuum level and thus a higher H β EW measurement. A systematic underestimation of the continuum level would result in a more pronounced effect for the EW of *broad* H β than it would for the EW of *narrow* [O III] λ 5007.

5.2. Correlations with Luminosity and Redshift

To determine whether any of the rest-frame optical emission properties correlated with luminosity or redshift, we computed the Spearman rank-order coefficients for the redshift and rest-frame *V*-band luminosity against the set of nine parameters common between both the low redshift and high redshift samples. The broad H β FWHM and α_{ox} of the $z \lesssim 0.5$ QSOs were tabulated in BG92, while the remaining parameters were measured by the fitting routine. As before, we also calculated the Kendall τ and found the results to be consistent. For the total combined $z \lesssim 0.5$ and $z \sim 2$ sample of $N = 119$ objects, a significant correlation at the $\gtrsim 99.7\%$ confidence level corresponds to a coefficient of $|r_s| \gtrsim 0.285$. The number of correlated pairs, their coefficients and confidence levels, for all nine parameters with respect to luminosity and redshift, are presented in Table 9.

Table 9. Correlations with Luminosity and Redshift

Emission Property	$N_{\text{pairs}}^{\text{a}}$	$\log(L_{\nu}(V))$		Redshift	
		r_s	CL ^b	r_s	CL ^b
H β _{broad} FWHM	111	+0.710	> 99.99	+0.671	> 99.99
[O III] FWHM	110	+0.703	> 99.99	+0.662	> 99.99
Fe II EW	109	+0.098	< 90.00	+0.073	< 90.00
Fe II/H β	109	+0.084	< 90.00	+0.074	< 90.00
H β EW	118	-0.103	< 90.00	-0.136	< 90.00
[O III] EW	116	-0.203	97.15	-0.208	97.47
[O III]/H β	115	-0.214	97.81	-0.194	96.20
Peak λ 5007	115	-0.130	< 90.00	-0.113	< 90.00
α_{ox}	80	-0.071	< 90.00	-0.083	< 90.00

^aFrom a total sample of 87 ($z < 0.5$) QSOs from BG92, added to our sample of 32 ($2.0 < z < 2.5$) QSOs.

^bConfidence Level

We find that the rest-frame FWHM of [O III] λ 5007 is positively correlated with luminosity, as well as redshift, at the $> 99.99\%$ confidence level. Figure 11a shows a clear trend where the forbidden narrow line width increases with the continuum luminosity emitted from the same spectral range. However, the lack of high redshift, low luminosity (*e.g.* $30 \leq \log(L_\nu(V)) \leq 32$) QSOs in our sample prevent us from distinguishing which property, redshift or luminosity, [O III] width physically depends upon.

Furthermore, we find a similar luminosity and redshift dependency for the rest-frame broad H β FWHM at $> 99.99\%$ significance. Again, the line width increases with the luminosity emitted at similar wavelengths (see Figure 11b), but in this case it is an allowed transition from the BELR which is firmly established to be physically distinct and distant from the NLR. As with our narrow line result, this relation could be biased by our selection of only high luminosity QSOs at $z > 2$. In a sample of 41 RLQs, Brotherton (1996) found a [O III] FWHM correlation with increasing rest-frame V luminosity; however, he did not find a like relation for H β FWHM and suggested that this was evidence for different line-broadening mechanisms in the BELR and NLR. Similar tests for same wavelength range luminosity dependencies of emission line widths have been done for the rest-frame UV with mixed results. One study showed a positive correlation between the FWHM of three broad emission lines (Ly α , N V, and C IV) and the luminosity emitted at 1450 Å, in a $z > 3$ QSO sample, but not in a $z > 2$ sample (Osmer, Porter & Green 1994), while another study showed only Ly α FWHM dependent on UV luminosity at $z < 1.5$ (Green 1996). At $z < 0.8$ the Ly α full-width at zero-intensity (FWZI) correlated with the luminosity emitted at 1549 Å (Corbin & Boroson 1996), yet the FWHMs of Ly α , C IV, and H β were all independent of this luminosity. Two other samples at $z \leq 2$ showed no correlations between emission line widths and luminosity emitted at UV wavelengths (Corbin 1992; and Brotherton *et al.* 1994a).

5.3. Baldwin Effects

An important emission line luminosity dependence observed in QSOs, is the systematic decrease in line EW with increasing continuum luminosity. This effect was first seen in the C IV λ 1549 line by Baldwin (1977), and has been found to extend over a wide range of luminosities in a large sample (Kinney, Rivolo & Koratker 1990). The “Baldwin Effect” has also been found in other rest-frame UV lines such as Ly α , N V, O VI, He II, C III], and Mg II (*e.g.* Tytler & Fan 1992; Green 1996). Furthermore, this trend has been shown to be continuous over all redshifts up to $z = 3.8$ for the C IV and Ly α lines (Osmer, Porter & Green 1994).

For the three rest-frame optical emission line EWs that we correlated with optical continuum luminosity (see Table 9), we noticed a weak ($\sim 97\%$ confidence) “Baldwin-like” trend for the [O III] λ 5007 line and no trend for H β or Fe II. However, since we found the EW of the [O III] line to correlate positively with radio strength (see §4.1), we split the total QSO sample into RQQ and RLQ subsamples and re-computed the Spearman rank-order coefficients against the rest-frame V -band luminosity. For the RQQ-only subsample of 87 objects, we found a more

significant ($\gtrsim 99\%$, $r_s = -0.291$) [O III] Baldwin Effect, with no effect present in the RLQ-only subsample. In particular, the absence of luminous, high redshift RQQs with EWs larger than 30 \AA is apparent in Figure 11c. Again, we must caution the reader that the EW of [O III] is equally well anti-correlated with redshift in the RQQ-only subsample, and that the lack of low luminosity, high redshift QSOs in this combined sample prevent the dis-entanglement of these two properties. In addition, we did not observe a Baldwin Effect for the $H\beta$ or Fe II lines, in either of the subsamples.

6. RLQ vs. RQQ Comparison

One of the main objectives of this study was to determine if there were significant differences between RLQs and RQQs in their rest-frame optical spectra. With the set of derived emission line parameters in hand, combined with the data from the literature, we constructed 22 distributions of the individual property’s values for the RLQ and RQQ subsamples. We calculated the mean of each property set, plus the right (+) and left (–) 1σ uncertainties in the mean via bootstrap re-sampling (see Press *et al.* 1992). Next, we calculated the two-sided Kolmogorov-Smirnov (K-S) probability that we could reject the null hypothesis that the RLQ and RQQ distributions of a given parameter were drawn from the same parent sample. The results of our comparison, including the number of objects, mean with associated 1σ uncertainties, and K-S test probabilities for each pair of RLQ and RQQ property distributions are tabulated in Table 10. Notice that the two subsamples are well matched in mean intrinsic luminosity ($L_\nu(V)$); therefore, parameter differences dependent on luminosity should be ruled out. We tested the validity of the K-S test under these conditions of limited numbers (typically 15 vs. 17) and determined that a difference probability of 97.8% is repeatable to within $\pm 0.3\%$. We find four independent properties different at $> 97.8\%$ confidence, and these results are plotted in Figures 12a – 12d. The top panel of each figure shows the RLQ distribution, while the RQQ distribution with its over-plotted BALQSO subsample is given in the bottom panel. The bin sizes approximate twice the mean of the individual 1σ values from the Monte Carlo error analysis. The large solid dots represent the mean of each distribution, and the uncertainties (1, 2 and 3 σ ’s) of each mean are given by the diminishing error bars. Note that one property, the measure of radio loudness ($\log(R')$) plotted in Figure 12a, shows a clear bimodal RLQ/RQQ distribution due to the choice of samples. The other three differences are discussed in detail below.

Table 10. RLQ vs. RQQ Emission Property Comparison

Emission Property	RLQ Distribution		RQQ Distribution		(%) diff ^a
	<i>N</i>	Mean	<i>N</i>	Mean	
[O III] EW (Å)	15	20.6 ^{+2.6} _{-3.5}	17	10.2 ^{+1.9} _{-1.7}	97.212
Hβ EW (Å)	14	64.8 ^{+6.2} _{-6.9}	17	73.2 ^{+5.1} _{-3.7}	57.072
Fe II EW (Å)	14	25.6 ^{+4.8} _{-4.9}	17	34.4 ^{+3.8} _{-4.2}	58.842
[O III] FWHM (km s ⁻¹)	14	1160 ⁺⁹⁰ ₋₈₀	15	1150 ⁺¹²⁰ ₋₁₃₀	32.185
Hβ total FWHM (km s ⁻¹)	14	4430 ⁺⁵⁹⁰ ₋₅₂₀	17	5100 ⁺³⁵⁰ ₋₄₇₀	62.250
Hβ broad FWHM (km s ⁻¹)	14	9870 ⁺⁹³⁰ ₋₉₇₀	17	11890 ⁺⁴⁵⁰ ₋₆₀₀	97.807
[O III]/Hβ	14	0.31 ^{+0.04} _{-0.05}	17	0.16 ^{+0.03} _{-0.05}	99.906
Fe II/Hβ	14	0.45 ^{+0.10} _{-0.09}	17	0.49 ^{+0.06} _{-0.06}	31.245
Peakλ5007	14	1.14 ^{+0.12} _{-0.14}	17	0.79 ^{+0.21} _{-0.26}	99.906
<i>z</i> _{sys}	15	2.207 ^{+0.032} _{-0.038}	17	2.222 ^{+0.029} _{-0.033}	38.978
log(<i>R'</i>)	15	3.042 ^{+0.144} _{-0.163}	17	0.198 ^{+0.076} _{-0.065}	100.000
log(<i>L</i> _ν (<i>V</i>)) (ergs s ⁻¹ Hz ⁻¹)	15	32.30 ^{+0.07} _{-0.08}	17	32.30 ^{+0.05} _{-0.05}	52.235
<i>V</i> magn	15	16.94 ^{+0.20} _{-0.20}	17	17.06 ^{+0.19} _{-0.16}	4.611
<i>H</i> magn	15	15.16 ^{+0.18} _{-0.25}	17	15.17 ^{+0.13} _{-0.12}	52.235
log(<i>L</i> _ν (2keV)) (ergs s ⁻¹ Hz ⁻¹)	13	28.58 ^{+0.10} _{-0.11}	12	27.95 ^{+0.22} _{-0.15}	98.701
<i>α</i> _{ox}	13	1.27 ^{+0.06} _{-0.05}	12	1.49 ^{+0.06} _{-0.04}	88.476
C IV FWHM (km s ⁻¹)	15	4880 ⁺³⁹⁰ ₋₄₆₀	15	6020 ⁺⁶⁷⁰ ₋₅₀₀	69.206
C III] FWHM (km s ⁻¹)	12	6430 ⁺⁷²⁰ ₋₇₃₀	14	8420 ⁺⁶²⁰ ₋₆₂₀	91.474
L _γ α EW (Å)	11	72.2 ^{+8.9} _{-8.3}	6	99.2 ^{+9.0} _{-8.0}	88.945
C IV EW (Å)	13	22.6 ^{+3.4} _{-3.4}	13	20.0 ^{+2.2} _{-2.5}	53.288
C III] EW (Å)	10	17.9 ^{+1.6} _{-1.6}	13	17.9 ^{+0.7} _{-0.7}	26.370
Mg II EW (Å)	7	23.1 ^{+2.3} _{-2.3}	6	29.1 ^{+4.1} _{-4.0}	9.339

^aTwo-sided K-S probability that the RLQ and RQQ distributions of a given property were not drawn from the same parent sample.

6.1. [O III] Strength Difference

We find that all measures of [O III] λ 5007 emission are stronger in the RLQ subsample than in the RQQ subsample at $\geq 97.2\%$ confidence. The [O III]/H β distributions are plotted for comparison in Figure 12b, notice that the RLQ and RQQ sample means do not intersect within the 1σ errors. BG92 found a similar, yet much weaker, result. A manifestation of this result was already illustrated by the strong positive correlation between [O III] strength and $\log(R')$ presented in §4.1. We propose that narrow [O III], in RLQs at least, is in fact emitted from a non-spherically symmetric region and that its strength is physically tied to the strong radio emission, perhaps the NLR ionization is anisotropic due to preferential continuum emission aligned with the radio axis (Bower *et al.* 1995; Simpson *et al.* 1996; and Wilson 1997). The correlation between [O III] strength and the ionizing continuum slope α_{ox} (also in §4.1) may be evidence for this idea.

6.2. Broad H β Width Difference

We find that the H β broad component FWHM is narrower in the RLQ subsample, at the 97.8% confidence level, compared to the RQQ subsample (see Figure 12c). Notice again that the means do not overlap within the 1σ errors. Many higher redshift samples have shown that RLQs have narrower BELR high ionization species, such as C IV and Ly α (*e.g.* Corbin 1991; and FHI93), than RQQs. However, one low redshift study found RLQs to have wider, rather than narrower, H β profiles than RQQs (Corbin & Boroson 1996). It has been shown that the H β line width is anti-correlated with viewing angle for QSOs in general (Wills & Brotherton 1995; and Baker & Hunstead 1995), and we corroborate this with the H β_{broad} FWHM – α_{ox} and H β_{broad} FWHM – $\log(L_{\nu}(V))$ correlations of §4.2. Yet if one assumes that [O III] strength is a measure related to radio loudness, then the strong [O III] strength – broad H β width anti-correlation (§4.1) suggests an additional factor in the broad Balmer width difference we observe. It would seem that the width of this line is dependent upon orientation for both RLQs and RQQs, but that it is also governed, to a lesser degree, by the mechanism that controls radio loudness.

6.3. Other Significant Differences

We find that the line width of the C III] λ 1909 emission is narrower in RLQs than RQQs. Though this result is $< 95\%$ confident, the difference between the means of the two sets is quite large ($\sim 2000 \text{ km s}^{-1}$) and statistically compelling — no overlap of the 1σ error bars. This result has been strongly confirmed in many other studies (Corbin 1991; Wills *et al.* 1993; Brotherton *et al.* 1994a; Corbin & Francis 1994; and Vestergaard, Wilkes & Barthel 1997; but not found by FHI93).

Finally, we find that soft X-ray luminosity (see Figure 12d) is significantly (98.7%) greater,

and that the mean optical-to-X-ray slope is somewhat flatter and harder in RLQs compared to RQQs. This result agrees well with the findings of a large sample study of Green (*et al.* 1995).

6.4. Important Null Result

The optical Fe II EW distributions are not statistically different between radio types, but the means of the two distributions are different at the 1σ level, such that RLQs have less Fe II emission than RQQs (see Figure 12e). This has been found in lower redshift ($z < 0.8$) samples (BG92 and Corbin & Boroson 1996). As mentioned in §4.1, BG92 suggest that the strength of Fe II is tied to some unknown property governing radio loudness and thus the two types of QSOs are physically different.

7. BALQSO vs. nonBALQSOs

To determine whether BALQSOs differed significantly from other radio quiet nonBALQSOs, we performed essentially the same analysis as described in §6 on two subsets drawn from the RQQ subsample. BALQSO membership (see Table 2) was based upon classifications by Turnshek (1984), WMFH91, and Thompson *et al.* (1989). Due to insufficient data points, we dropped the Ly α and Mg II λ 2798 EW distributions. The results of our comparative analysis are presented, as before, in Table 11. Again, we tested the validity of the K-S test under these conditions of even smaller numbers (typically 7 vs. 10) and found that a difference probability of 91.6% is repeatable to within $\pm 1.5\%$. We find no statistically significant ($\geq 95\%$) differences between any BALQSO and nonBALQSO optical emission property subsets measured from our sample. One property, the EW of the C IV λ 1549 is less in the BALQSO subset at $> 99.6\%$ significance, even though all but one of the BALQSOs making up this subset were classified as having “detached” blueward C IV absorption, there is still an issue of its contamination of the C IV emission.

Table 11. NonBALQSO vs. BALQSO Emission Property Comparison

Emission Property	NonBALQSO Distribution		BALQSO Distribution		(% diff) ^a
	<i>N</i>	Mean	<i>N</i>	Mean	
[O III] EW (Å)	10	11.6 ^{+2.1} _{-2.2}	7	8.1 ^{+2.6} _{-2.1}	32.896
Hβ EW (Å)	10	74.5 ^{+5.8} _{-5.5}	7	71.5 ^{+7.5} _{-7.3}	48.550
Fe II EW (Å)	10	27.8 ^{+5.3} _{-5.6}	7	43.9 ^{+6.5} _{-7.1}	84.672
[O III] FWHM (km s ⁻¹)	10	1130 ⁺¹⁸⁰ ₋₁₇₀	5	1200 ⁺¹⁴⁰ ₋₁₅₀	13.811
Hβ _{total} FWHM (km s ⁻¹)	10	4560 ⁺⁶¹⁰ ₋₄₆₀	7	5870 ⁺⁵⁴⁰ ₋₆₇₀	73.771
Hβ _{broad} FWHM (km s ⁻¹)	10	11490 ⁺⁷³⁰ ₋₇₆₀	7	12460 ⁺⁶⁶⁰ ₋₁₀₂₀	27.632
[O III]/Hβ	10	0.19 ^{+0.07} _{-0.07}	7	0.12 ^{+0.04} _{-0.05}	48.550
Fe II/Hβ	10	0.38 ^{+0.06} _{-0.06}	7	0.64 ^{+0.11} _{-0.09}	91.605
Peakλ5007	10	0.94 ^{+0.40} _{-0.40}	7	0.58 ^{+0.21} _{-0.23}	66.549
<i>z</i> _{sys}	10	2.221 ^{+0.048} _{-0.046}	7	2.225 ^{+0.022} _{-0.020}	82.361
log(<i>R'</i>)	10	0.267 ^{+0.084} _{-0.091}	7	0.100 ^{+0.128} _{-0.143}	48.550
log(<i>L</i> _ν (<i>V</i>)) (ergs s ⁻¹ Hz ⁻¹)	10	32.32 ^{+0.07} _{-0.08}	7	32.27 ^{+0.06} _{-0.06}	22.525
<i>V</i> magn	10	16.88 ^{+0.24} _{-0.27}	7	17.32 ^{+0.18} _{-0.17}	22.525
<i>H</i> magn	10	15.11 ^{+0.18} _{-0.15}	7	15.26 ^{+0.12} _{-0.11}	22.525
log(<i>L</i> _ν (2keV)) (ergs s ⁻¹ Hz ⁻¹)	7	28.16 ^{+0.20} _{-0.17}	5	27.65 ^{+0.21} _{-0.21}	90.923
α _{ox}	7	1.43 ^{+0.06} _{-0.06}	5	1.57 ^{+0.09} _{-0.09}	55.721
C IV FWHM (km s ⁻¹)	8	6330 ⁺⁸⁰⁰ ₋₆₆₀	7	5650 ⁺⁹⁷⁰ ₋₇₄₀	13.918
C III] FWHM (km s ⁻¹)	9	8100 ⁺⁵⁸⁰ ₋₆₆₀	5	8990 ⁺¹³¹⁰ ₋₉₁₀	63.599
C IV EW (Å)	8	25.3 ^{+2.6} _{-1.8}	6	13.1 ^{+1.3} _{-1.5}	99.639
C III] EW (Å)	8	18.1 ^{+0.6} _{-0.7}	5	17.6 ^{+1.9} _{-1.9}	41.425

^aTwo-sided K-S probability that the RLQ and RQQ distributions of a given property were not drawn from the same parent sample.

7.1. Possible Differences

We find that the BALQSO subset has stronger optical Fe II emission than the nonBALQSO subset (see Figure 12e). This difference is obvious in both the Fe II/H β and Fe II EW pairs of means. It has been found that loBALs, in particular, are stronger in Fe II, as well as weaker in [O III], compared with nonBALQSOs (Boroson & Meyers 1992; Turnshek *et al.* 1994; and Wills & Brotherton 1996); however, our BALQSO subset contains only one known loBAL (Q1011+091 – WMFH91). A visual inspection of this object’s rest-frame optical spectrum shows that it is indeed Fe II rich, as well as [O III] weak. Yet, the same can be said for known hiBALs Q1246-057 and Q1309-056, as well as known radio quiet nonBALQSOs Q0049+007 (UM287) and Q1346-036, while other BALQSOs like Q0043+008 (UM275 – known hiBAL) and Q2212-179 (unknown BAL type) show the inverse trend of weak Fe II and strong [O III] emission, common among most of the nonBALQSO subsample. Thus it appears that the [O III] – Fe II anti-correlation of §4.1 is valid for *all* QSO classifications, but no distinction between loBALs and hiBALs is apparent in our data. Whether these statistically weak results point towards any differences, physical or aspect dependent, between BALQSOs and nonBALQSOs is not clear. A larger sample with better S/N might shed some light on this. We can only say that at the sensitivity of our observations, the BALQSO and radio quiet nonBALQSO subsamples appear similar in their optical rest-frame spectral properties.

We also find that BALQSOs are somewhat weaker in soft X-ray luminosity (see Figure 12d) as confirmed by Turnshek (1984), and Green & Mathur (1996a). It has been suggested that strong absorption from the dense BAL clouds is responsible for the weaker X-ray flux (Green *et al.* 1995; and Murray *et al.* 1995).

8. Summary

We have presented a detailed study of the emission line properties of 32 high luminosity QSOs at high redshift, drawing on new *H*-band spectra. Of the sample members, 15 are classified as RLQ and 17 are RQQ, but both are similar in redshift and luminosity distributions. The spectral coverage for the entire sample included the forbidden [O III] $\lambda\lambda$ 4959, 5007 narrow lines, the allowed Balmer H β broad line, and the blended optical Fe II broad emission in the neighborhood of H β . We caution the reader that even though our data are allowing an unprecedented view of the rest-frame optical spectrum in luminous, high redshift QSOs, the data are still of low S/N and only moderate spectral resolution. The summary of our findings follows:

1. We find that, aside from their radio properties, the RLQ and RQQ subsets are significantly (> 97.2%) different in several observables, implying that the two types come from intrinsically separate populations of QSOs.
2. At the sensitivity of our observations, we find no statistically significant (> 95%) differences

between any rest-frame optical emission line properties, of the BALQSO and nonBALQSO subsets drawn from the radio quiet subsample. This is consistent with the hypothesis that any observed differences on an object-to-object basis can be explained by a combination of BAL cloud covering factor and orientation.

3. We report a previously unknown possible luminosity dependency of the forbidden [O III] λ 5007 NLR emission velocity width over the range $0 < z < 2.5$. In addition, we confirm a similar dependency for the $H\beta$ broad line width. We propose that these findings might be evidence for a physical connection between the continuum and line emitting regions at similar energies. Furthermore, we report a [O III] λ 5007 “Baldwin Effect” for the RQQ-only sample over this same redshift range.

9. Discussion

The most significant correlation we found is the RLQ-RQQ dichotomy. To put our observations into context we present a model, largely drawing on existing work, illustrating the physical differences supported by the majority of the significant correlations found in this statistical study. For the RLQ population we assume the “standard model” for the central power source — a super-massive black hole and associated accretion disk that produces the ionizing continuum, from thermal soft X-rays to UV photons (Laor *et al.* 1997). A powerful, relativistic, and tightly collimated jet of synchrotron radio flux (Stoche *et al.* 1992) is emitted roughly perpendicular to the accretion disk. The existence of this jet explains why RLQs are ~ 1000 times more radio luminous than RQQs. An extra component of harder X-rays is produced by inverse Compton scattering of some of the beamed radio emission (Elvis *et al.* 1994; and Green *et al.* 1995). The existence of this additional X-ray component explains why RLQs are somewhat more X-ray bright, and why their ionizing continuum is flatter than in RQQs. We assume that this component strengthens and hardens the ionizing continuum preferentially near the radio jet axis. Surrounding the central engine are the BELR clouds in a semi-flattened, gravitationally bound system (Jackson & Browne 1991). For RLQs we adopt the VBLR+ILR model proposed by Wills and Brotherton (see Wills *et al.* 1993; Brotherton *et al.* 1994a; etc.), such that emission from the VBLR is equivalent to the broad ($v_{FWHM} \sim 10^4$ km s $^{-1}$) component of emission from the BELR, and that the VBLR is stratified with the highest ionization species closest to the nucleus (Baldwin 1997). Extending away from the VBLR, we assume the existence of bipolar ionization cones roughly aligned with the radio axis as seen in some low redshift Seyfert galaxies (*e.g.* Simpson *et al.* 1996). At the apex of each cone is the low velocity ($v_{FWHM} \sim \text{few}10^3$ km s $^{-1}$) ILR that we assume is also stratified. Finally, further outward, at the wider end of each cone, is the non-spherically symmetric NLR.

The statistical differences between RLQs and RQQs, as well as many significant correlations between emission properties, found in this study can be explained in the context of our proposed RLQ model as follows:

- (i) The more strongly collimated continuum emission photo-ionizing a greater volume of NLR gas, that is concentrated in a non-spherically symmetric region, could produce the stronger [O III] emission observed in RLQs compared to RQQs.
- (ii) As with the NLR, we argue that an increased flux from the ILR is expected, due to more completely ionized gas by the collimated continuum focused on a tight region at the apex of the bipolar ionization cones. Permitted C III] and C IV emission originating in sufficient amounts from the ILR could produce the overall narrower line widths seen in RLQs relative to RQQs, as well as explain the two inverse correlations between [O III] strength and the widths of C III] and C IV, and the positive relation between [O III] EW and C IV EW.
- (iii) The association between the existence of the radio jet and the production of the more powerful and harder ionizing continuum can physically explain why $\log(R')$ and α_{ox} are anti-correlated. Coupling the preceding idea with (i) should produce the observed positive [O III] strength – $\log(R')$ and negative [O III] strength – α_{ox} relations.
- (iv) The broad component of the H β , C III] and C IV emission lines is presumed to come from the VBLR, while a significant flux from the ILR makes up the remaining component of the C IV and C III] broad-emission-lines. Thus, one should expect the strong C IV FWHM – C III] FWHM correlation observed, in addition to weaker correlations between the *total* line widths of the carbon ions and H β_{broad} FWHM.
- (v) Assuming α_{ox} is a measure of viewing angle with respect to the radio jet axis, then the H β_{broad} FWHM – α_{ox} correlation may be evidence of a gravitationally bound VBLR. Furthermore, assuming the luminosity is directly related to the mass of the central massive black hole, an increase in luminosity should correlate, on average, with an increase in line width as observed in the H β FWHM – $\log(L_{\nu}(V))$ relation.

The above discussion was aimed towards an explanation of the RLQ population properties. The RQQ version of our model differs in its lack of a strong, collimated radio jet. Thus, we argue that though RQQs have a similar nuclear source in mass and accretion rate as the RLQ population (Hooper *et al.* 1996), but instead of a collimated jet, the RQQs produce a sub-relativistic, uncollimated wind (Stoche *et al.* 1992), or a weak, non-boosted jet (Falcke, Sherwood & Patnaik 1996). This proposed model has several implications:

- (i) Assuming there is a connection between the increased coverage of optically thick, iron emitting VBLR clouds, and the lack of a strong, collimated radio jet, the VBLR covering factor in RQQs should be larger, increasing the shielding of ionizing photons to the NLR (Wills 1996), as well as the ILR.
- (ii) Combining the increased shielding of ionizing radiation to the ILR and NLR with the absence of an additional hard, collimated component of thermal soft X-rays in RQQs, may enhance

emission from low ionization species like Fe^+ in the VBLR, while diminishing emission from higher ionization species in the ILR and NLR.

These two effects could be responsible for the observed negative correlation between [O III] strength and Fe II strength, plus the $\text{H}\beta$ EW and Fe II EW correlations with α_{ox} , and the C IV and C III] line width to Fe II strength relations.

We would like to thank George Rieke for useful discussion and help in obtaining these data. Fred Chaffee is thanked for a generous allotment of Director's time on the MMT. Todd Boroson kindly made his spectra of the low redshift sample available in digital form, as well as the optical Fe II template from I Zw 1. We thank Bev Wills for faxing us a UV rest spectrum of Q2310+385. We acknowledge helpful discussions and correspondence with Gary Schmidt, Jim Condon, Jill Bechtold, Eric Hooper, and Pat Hall. We are grateful to Chad Engelbracht and Kevin Luhman for answering endless data reduction questions. And we thank Margaret Hanson for help with atmospheric corrections. This research has made use of the NASA/IPAC Extragalactic Database (NED) which is operated by the Jet Propulsion Laboratory, California Institute of Technology, under contract with the National Aeronautics and Space Administration. We also made use of NASA's Astrophysical Data System Abstract Service (ADS). We acknowledge support from NSF grant (AST93-20715). Acquisition of the NICMOS3 array was made possible by NASA.

REFERENCES

- Adam, G. 1985, *A&AS*, **61**, 225
- Baker, A. C., Carswell, R. F., Bailey, J. A., Espey, B. R., Smith, M. G., and Ward, M. J. 1994, *MNRAS*, **270**, 575
- Baker, J. C., and Hunstead, R. W. 1995, *ApJ*, **452**, L95
- Baker, J. C. 1997, *MNRAS*, **286**, 23
- Baldwin, J. A. 1977, *ApJ*, **214**, 679
- Baldwin, J. A., Wampler, E. J., and Gaskell, C. M. 1989, *ApJ*, **338**, 630
- Baldwin, J., Ferland, G., Korista, K., and Verner, D. 1995, *ApJ*, **455**, L119
- Baldwin, J. 1997, in *Emission Lines in Active Galaxies: New Methods and Techniques*, ed. Peterson, B. M., Cheng, F.-Z., and Wilson, A. S. (Astronomical Society of the Pacific: San Francisco), p. 80
- Barvainis, R., Lonsdale, C., and Antonucci, R. 1996, *AJ*, **111**, 1431
- Becker, R. H., Gregg, M. D., Hook, I. M., McMahon, R. G., White, R. L., and Helfand, D. J. 1997, *ApJ*, **479**, L93
- Blandford, R. D., and McKee, C. F. 1982, *ApJ*, **255**, 419
- Blandford, R. D. 1990, in *Active Galactic Nuclei*, ed. Courvoisier, T. J.-L., and Mayor, M. (Springer-Verlag: Berlin), p. 161
- Boller, T., Brandt, W. N., and Fink, H. 1996, *A&A*, **305**, 53
- Boroson, T. A. & Green, R. F. 1992, *ApJS*, **80**, 109 (BG92)
- Boroson, T. A., and Meyers, K. T. 1992, *ApJ*, **397**, 442
- Bower, G., Wilson, A., Morse, J. A., Gelderman, R., Whittle, M., and Mulchaey, J. 1995, *ApJ*, **454**, 106
- Brinkmann, W., Yuan, W., and Siebert, J. 1997, *A&A*, **319**, 413
- Brotherton, M. S., Wills, B. J., Steidel, C. C., and Sargent, W. L. W. 1994a, *ApJ*, **423**, 131
- Brotherton, M. S., Wills, B. J., Francis, P. J., and Steidel, C. C. 1994b, *ApJ*, **430**, 495
- Brotherton, M. S. 1996, *ApJS*, **102**, 1

- Brotherton, M. S. 1997, in *Emission Lines in Active Galaxies: New Methods and Techniques*, ed. Peterson, B. M., Cheng, F. -Z., and Wilson, A. S. (Astronomical Society of the Pacific: San Francisco), p. 258
- Burbidge, G., and Burbidge, M. 1967, *Quasi-stellar Objects*, (W. H. Freeman: San Francisco), p.112
- Campins, H., Rieke, G. H., and Lebofsky, M. J. 1985, *AJ*, **90**, 896
- Carswell, R. F. *et al.* 1991, *ApJ*, **381**, L5
- Cimatti, A., Freudling, W., Röttgering, H. J. A., Ivison, R. J., and Mazzei, P. 1998, *A&A*, **329**, 399
- Clavel, J. *et al.* 1991, *ApJ*, **366**, 64
- Cohen, M. H., Ogle, P. M., Tran, H. D., Vermeulen, R. C., Miller, J. S., Goodrich, R. W., and Martel, A. R. 1995, *ApJ*, **448**, L77.
- Condon, J. J., Cotton, W. D., Greisen, E. W., Yin, Q. F., Perley, R. A., Taylor, G. B., and Broderick, J. J. 1996, NCSA Astron. Dig. Image Libr. (NRAO VLA Sky Survey)
- Corbin, M. R. 1991, *ApJ*, **375**, 503
- Corbin, M. R. 1992, *ApJ*, **391**, 577
- Corbin, M. R., and Francis, P. J. 1994, *AJ*, **108**, 2016
- Corbin, M. 1995, *ApJ*, **447**, 496
- Corbin, M. R., and Boroson, T. A. 1996, *ApJS*, **107**, 69
- Crawford, C. S., and Vanderriest, C. 1997, *MNRAS*, **285**, 580
- di Serego Alighieri, S., Cimatti, A., Fosbury, R. A. E., and Hes, R. 1997, *A&A*, **328**, 510
- Elvis, M., Wilkes, B. J., McDowell, J. C., Green, R. F., Bechtold, J., Willner, S. P., Oey, M. S., Polomski, E., and Cutri, R. 1994, *ApJS*, **95**, 1
- Falcke, H., Sherwood, W., and Patnaik, A. R. 1996, *ApJ*, **471**, 106
- Ferland, G. J., Peterson, B. M., Horne, K., Welsh, W. F., and Nahar, S. N. 1992, *ApJ*, **387**, 95
- Filippenko, A. V., and Halpern, J. P. 1984, *ApJ*, **285**, 458
- Francis, P. J., Hewett, P. C., Foltz, C. B., Chaffee, F. H., Weymann, R. J., and Morris, S. L. 1991, *ApJ*, **373**, 465
- Francis, P. J., Hooper, E. J., and Impey, C. D. 1993, *AJ*, **106**, 417 (FHI93)

- Glenn, J., Schmidt, G. D., and Foltz, C. B. 1994, *ApJ*, **434**, 47
- Goodrich, R. W., and Miller, J. S. 1995, *ApJ*, **448**, L73
- Green, P. J., Schartel, N., Anderson, S. F., Hewett, P. C., Foltz, C. B., Brinkmann, W., Fink, H., Trümper, J., and Margon, B. 1995, *ApJ*, **450**, 51
- Green, P. J., and Mathur, S. 1996, *ApJ*, **462**, 637
- Green, P. J. 1996, *ApJ*, **467**, 61
- Gregory, P. C., and Condon, J. J. 1991, *ApJS*, **75**, 1011 (GB87 Survey)
- Gregory, P. C., Scott, W. K., Douglas, K., and Condon, J. J. 1996, *ApJS*, **103**, 427 (GB6 Survey)
- Hall, P. B., Ellingson, E., and Green, R. F. 1997, *AJ*, **113**, 1179
- Hamann, F., Korista, K. T., and Morris, S. L. 1993, *ApJ*, **415**, 541
- Hartig, G. F., and Baldwin, J. A. 1986, *ApJ*, **302**, 64
- Hewett, P. C., and Foltz, C. B., 1997, private communication
- Hewitt, A., and Burbidge, G. 1993, *ApJS*, **87**, 451
- Hill, G. J., Thompson, K. L., and Elston, R. 1993, *ApJ*, **414**, L1
- Hines, D. C., and Wills, B. J. 1995, *ApJ*, **448**, L69
- Hoffleit, D., and Jaschek, C. 1982, *The Bright Star Catalogue*, (Yale University: New Haven)
- Hooper, E. J., Impey, C. D., Foltz, C. B., and Hewett, P. C. 1995, *ApJ*, **445**, 62
- Hooper, E. J., Impey, C. D., Foltz, C. B., and Hewett, P. C. 1996, *ApJ*, **473**, 746
- Hyland, A. R., and Allen, D. A. 1982, *MNRAS*, **199**, 943
- Jackson, N., and Browne, I. W. A. 1991, *MNRAS*, **250**, 422
- Joly, M. 1991, *A&A*, **242**, 49
- Johnson, H. L. 1966, *ARA&A*, **4**, 193
- Johnston, K. J., *et al.* 1995, *AJ*, **110**, 880
- Kaspi, S., Smith, P. S., Maoz, D., Netzer, H., and Jannuzi, B. T. 1996, *ApJ*, **471**, L75
- Kellermann, K. I., Sramek, R., Schmidt, M., Shaffer, D. B., and Green, R. 1989, *AJ*, **98**, 1195
- Kinney, A. L., Rivolo, A. R., and Koratker, A. P. 1990, **357**, 338

- Kwan, J., and Krolik, J. H. 1981, *ApJ*, **250**, 478
- Laor, A., Fiore, F., Elvis, M., Wilkes, B. J., and McDowell, J. C. 1994, *ApJ*, **435**, 611
- Laor, A., Bahcall, J. N., Januzzi, B. T., Schneider, D. P., and Green, R. F. 1995, *ApJS*, **99**, 1
- Laor, A., Fiore, F., Elvis, M., Wilkes, B. J., and McDowell, J. C. 1997, *ApJ*, **477**, 93
- Laor, A. 1998, *ApJ*, **496**, L71
- Lawrence, C. L., Zucker, J. R., Readhead, A. C. S., Unwin, S. C., Pearson, T. J., and Xu, W. 1996, *ApJS*, **107**, 541
- Lipari, S. 1994, *ApJ*, **436**, 102
- Lonsdale, C. J., Barthel, P. D., and Miley, G. K. 1993, *ApJS*, **87**, 63
- Marziani, P., Sulentic, J. W., Dultzin-Hacyan, D., Calvani, M., and Moles, M. 1996, *ApJS*, **104**, 37
- McIntosh, D. H., Rix, H.-W., Foltz, C. B., Rieke, M. J., and Weymann, R. J. 1999, in prep.
- Miller, L., Peacock, J. A., and Mead, A. R. G. 1990, *MNRAS*, **244**, 207
- Murray, N., Chiang, J., Grossman, S. A., and Voit, G. M. 1995, *ApJ*, **451**, 498
- Neugebauer, G., Green, R. F., Matthews, K., Schmidt, M., Soifer, B. T., and Bennett, J. 1987, *ApJS*, **63**, 615
- Netzer, H., and Wills, B. J. 1983, *ApJ*, **275**, 445
- Osmer, P. S., Porter, A. C., and Green, R. F. 1994, *ApJ*, **436**, 678
- Osterbrock, D. E. 1989, *Astrophysics of Gaseous Nebulae and Active Galactic Nuclei* (University Science Books: Mill Valley), p. 119
- Peterson, B. M. *et al.* 1991, *ApJ*, **368**, 119
- Peterson, B. M. 1993, *PASP*, **105**, 247
- Peterson, B. M. 1997, *An Introduction to Active Galactic Nuclei* (Cambridge University Press: Cambridge)
- Press, W. H., Teukolsky, S. A., Vetterling, W. T., and Flannery, B. P. 1992, *Numerical Recipes in Fortran 77: The Art of Scientific Computing*, Second Edition, Vol. 1 (Cambridge University Press: Cambridge)
- Reimers, D., Bade, N., Schartel, N., Hagen, H.-J., Engels, D., and Toussaint, F. 1995, *A&A*, **296**, L49

- Rieke, M., and Weymann, R. 1995, private communication
- Rix, H.-W., Kennicutt, Jr., R. C., Braun, R., and Walterbus, R. A. M. 1995, ApJ, **438**, 155
- Sargent, W. L. W., Boksenberg, A., and Steidel, C. C. 1988, ApJS, **68**, 539
- Schartel, N., Walter, R., Fink, H. H., and Truemper, J. 1996, A&A, **307**, 33
- Schneider, D. P., Schmidt, M., and Gunn, J. E. 1994, AJ, **107**, 1245
- Simpson, C., Mulchaey, J. S., Wilson, A. S., Ward, M. J., and Alonso-Herrero, A. 1996, ApJ, **457**, L19
- Sitko, M. L., Stein, W. A., Zhang, Y. -X., and Wisniewski, W. Z. 1982, ApJ, **259**, 486
- Sprayberry, D., and Foltz, C. B. 1992, ApJ, **390**, 39
- Steidel, C. S., and Sargent, W. L. W. 1991, ApJ, **382**, 433
- Stickel, M., and Kühn, H. 1993, A&AS, **100**, 395
- Stickel, M., Meisenheimer, K., and Kühn, H. 1994, A&AS, **105**, 211
- Stoeckle, J. T., Morris, S. L., Weymann, R. J., and Foltz, C. B. 1992, ApJ, **396**, 487
- Thompson, D. J., Djorgovski, S., and Weir, W. N. 1989, PASP, **101**, 1065
- Turnshek, D. A. 1984, ApJ, **280**, 51
- Turnshek, D. A. *et al.* 1994, ApJ, **428**, 93
- Tytler, D., and Fan, X.-M. 1992, ApJS, **79**, 1
- Ulrich, M.-H. 1989, A&A, **220**, 71
- Vestergaard, M., Wilkes, B. J., and Barthel, P. D. 1997, in *Emission Lines in Active Galaxies: New Methods and Techniques*, ed. Peterson, B. M., Cheng, F. -Z., and Wilson, A. S. (Astronomical Society of the Pacific: San Francisco), p. 256
- Viegas, S. M., and Contini, M. 1997, in *Emission Lines in Active Galaxies : New Methods and Techniques*, ed. Peterson, B. M., Cheng, F. -Z., and Wilson, A. S. (Astronomical Society of the Pacific: San Francisco), p. 365
- Visnovsky, K. L., Impey, C. D., Foltz, C. B., Hewett, P. C., Weymann, R. J., and Morris, S. L. 1992, ApJ, **391**, 560
- Wang, T., Brinkmann, W., and Bergeron, J. 1996, A&A, **309**, 81
- Wang, T., Zhou, Y.-Y., and Gao, A.-S. 1996, ApJ, **457**, 111

- Weymann, R. J., Morris, S. L., Foltz, C. B., and Hewett, P. C. 1991, *ApJ*, **373**, 23 (WMFH91)
- Wilkes, B. J., Tananbaum, H., Worrall, D. M., Avni, Y., Oey, M. S., and Flanagan, J. 1994, *ApJS*, **92**, 53
- Wilkes, B. J., Green, P. J., Mathur, S., and McDowell, J. C. 1997, in *Emission Lines in Active Galaxies: New Methods and Techniques*, ed. Peterson, B. M., Cheng, F. -Z., and Wilson, A. S. (Astronomical Society of the Pacific: San Francisco), p. 126
- Williams, D. M., Thompson, C. L., Rieke, G. H., and Montgomery, E. F. 1993, *SPIE Proc.*, **1946**, 482
- Wills, B. J., Brotherton, M. S., Fang, D., Steidel, C. C., and Sargent, W. L. W. 1993, *ApJ*, **415**, 563
- Wills, B. J., and Brotherton, M. S. 1995, *ApJ*, **448**, L81
- Wills, B. J. 1996, in *Jets from Stars to Active Galactic Nuclei*, ed. Kundt, W. (Springer-Verlag: Berlin), p. 213
- Wills, B. J., and Brotherton, M. S. 1996, in *Jets from Stars to Active Galactic Nuclei*, ed. Kundt, W. (Springer-Verlag: Berlin), p. 203
- Wills, B. 1997, private communication
- Wilson, A. S., Braatz, J. A., Heckman, T. M., Krolik, J. H., and Miley, G. K. 1993, *ApJ*, **419**, L61
- Wilson, A. S., and Colbert, E. J. M. 1995, *ApJ*, **438**, 62
- Wilson, A. S. 1997, in *Emission Lines in Active Galaxies: New Methods and Techniques*, ed. Peterson, B. M., Cheng, F. -Z., and Wilson, A. S. (Astronomical Society of the Pacific: San Francisco), p. 264
- Wisotzki, L., Köhler, T., Kayser, R., and Reimers, D. 1993, *A&A*, **278**, L15
- Wolfe, A. M., Turnshek, D. A., Smith, H. E., and Cohen, R. D. 1986, *ApJS*, **61**, 249
- Woltjer, L. 1959, *ApJ*, **130**, 38
- Wright, A. E., and Otrupcek, R. E. 1990, PKSCAT90 Radio Source Catalog and Sky Atlas (Australia Telescope National Facility) (the 1990 Parkes 8.4GHz Survey)

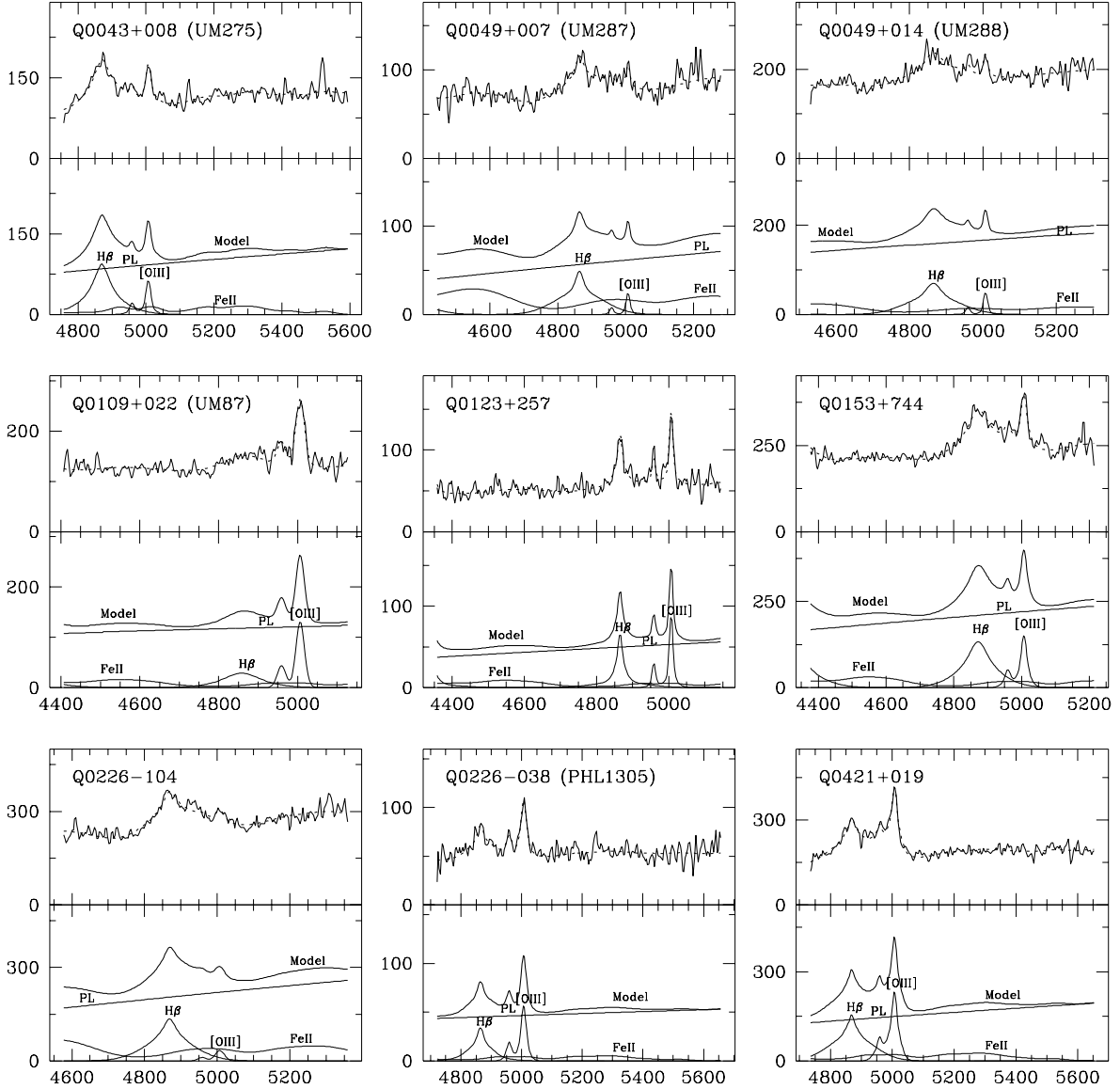
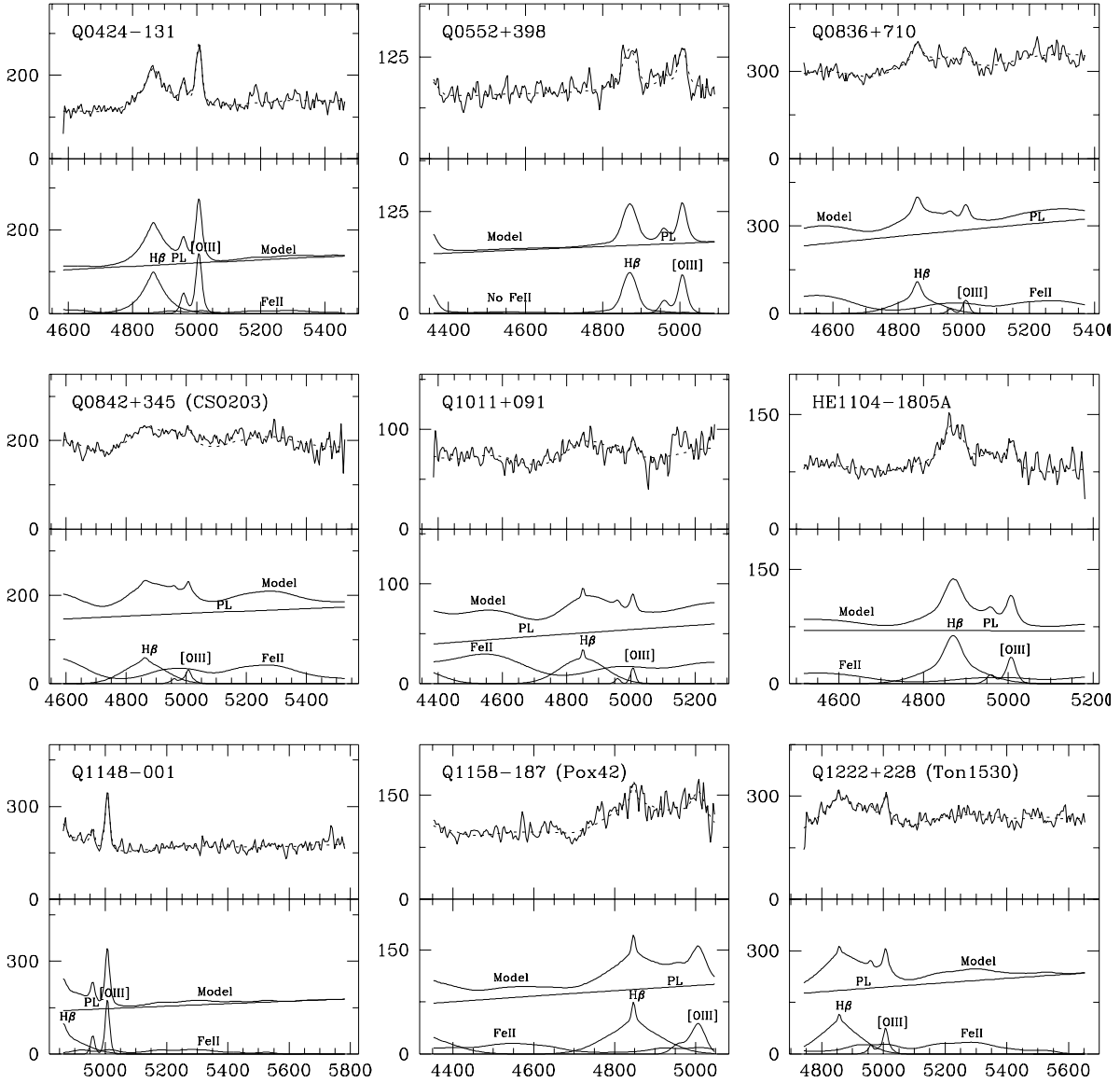
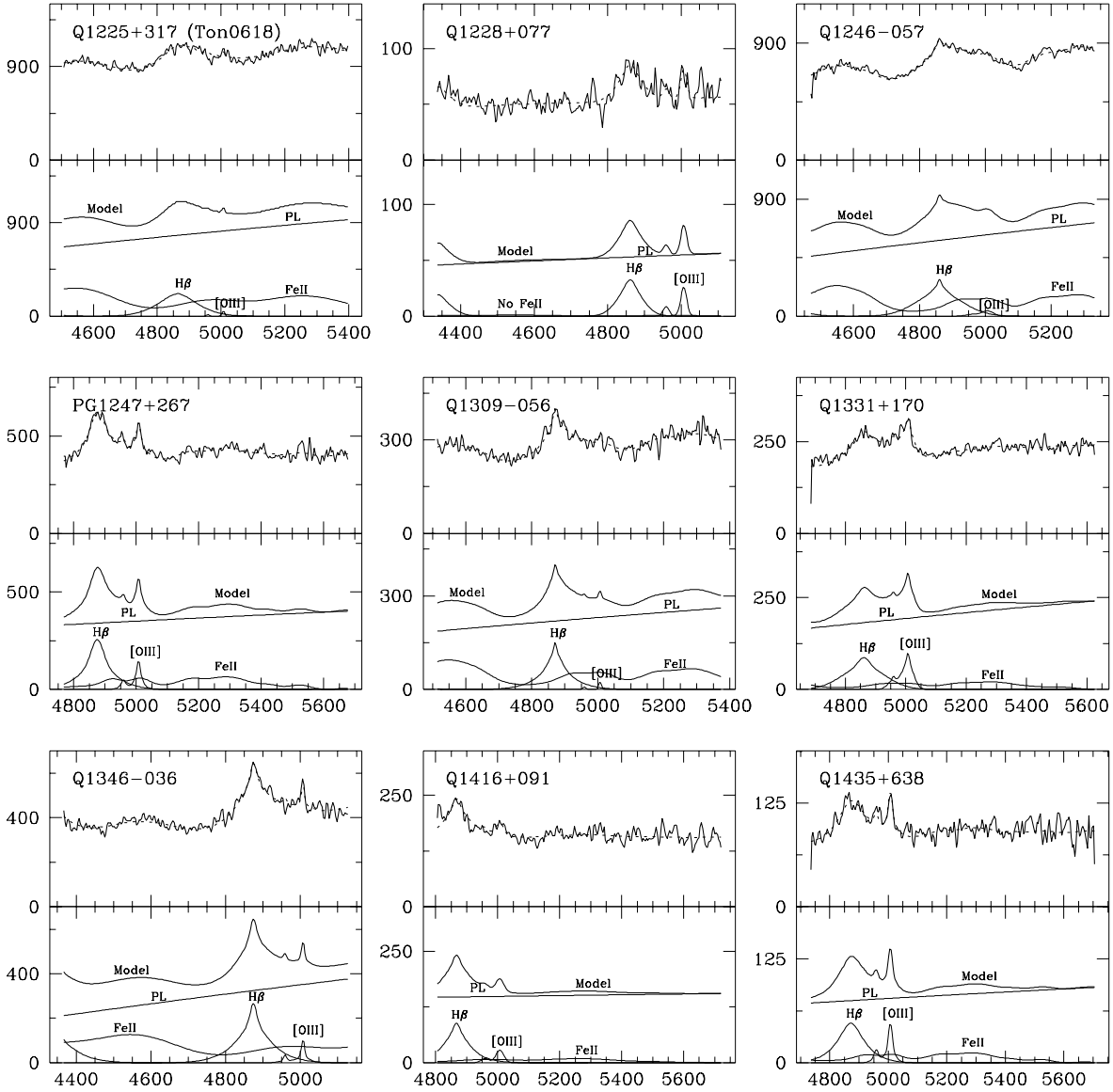
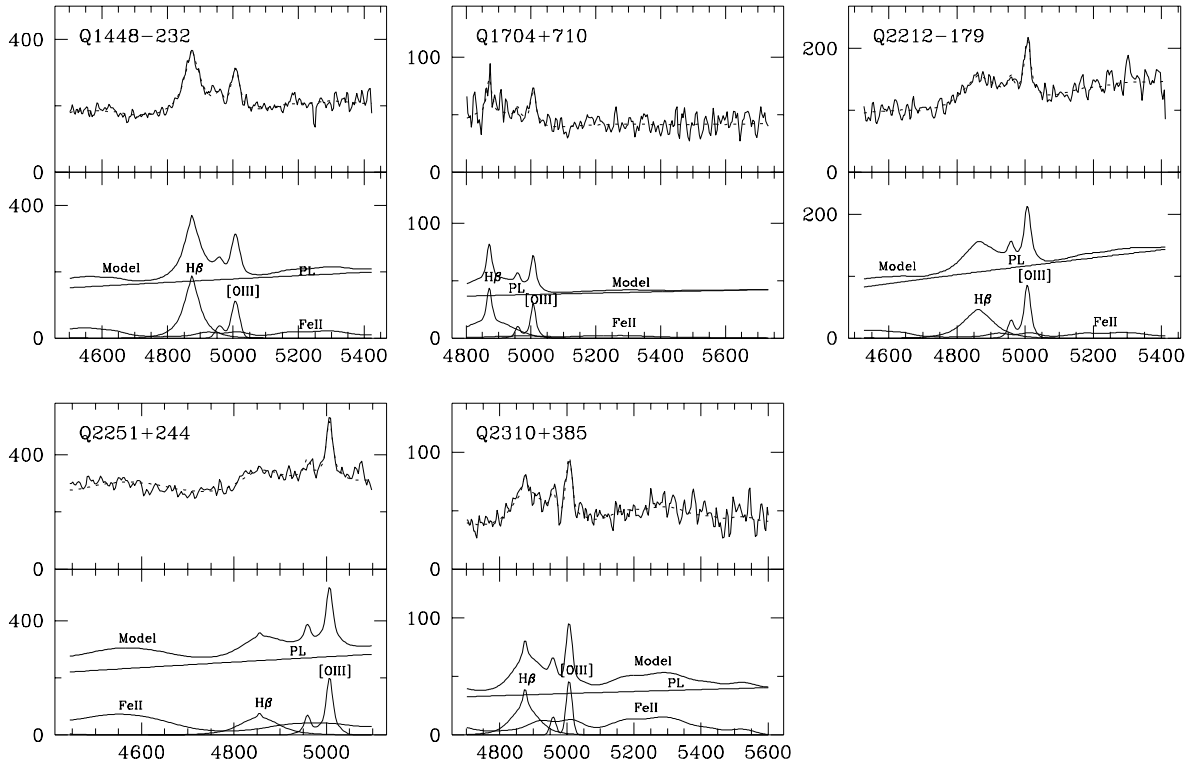


Fig. 1.— Rest-frame spectra of all 32 QSOs with their minimized χ^2 best fit model (dashed line) in top panel. The lower panel shows the model (bold line) with its H β , [O III], Fe II and power-law components. The horizontal axis is wavelength in \AA , while the vertical axis shows flux levels in arbitrary units.







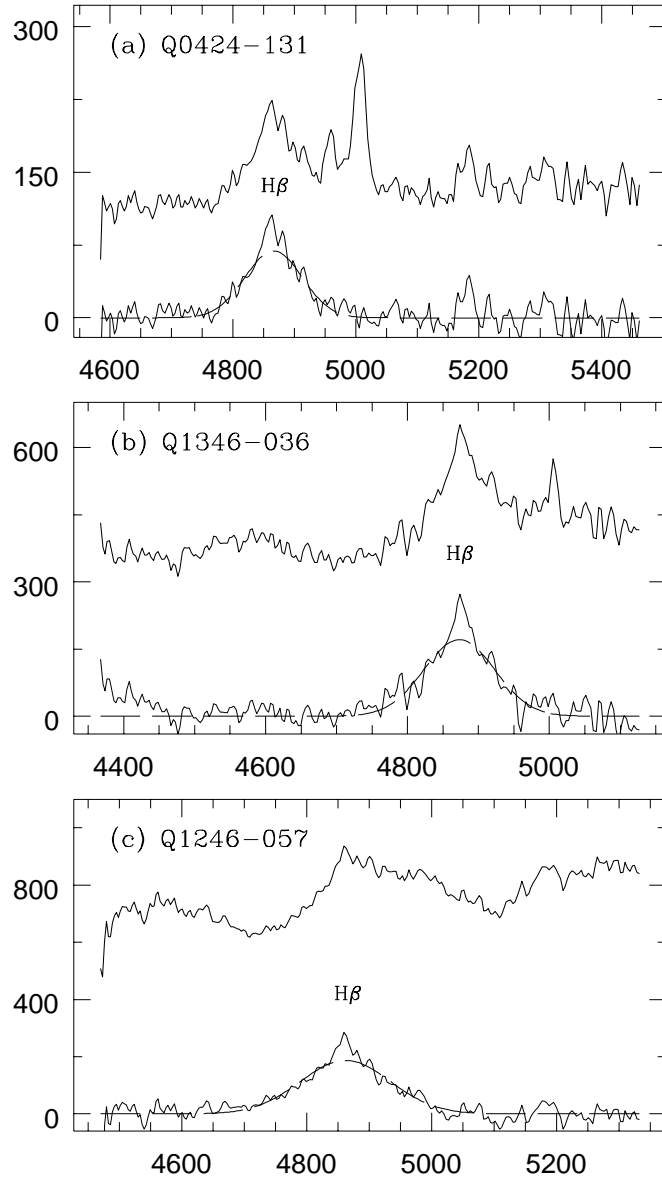


Fig. 2.— Representative examples of a rest-frame spectrum (upper), with extracted H β line (lower), and single Gaussian *broad* component fit (dashed). For: (a) a RLQ; (b) a RQQ; and (c) a BALQSO. The horizontal axis is wavelength in Å, while the vertical axis shows flux levels in arbitrary units.

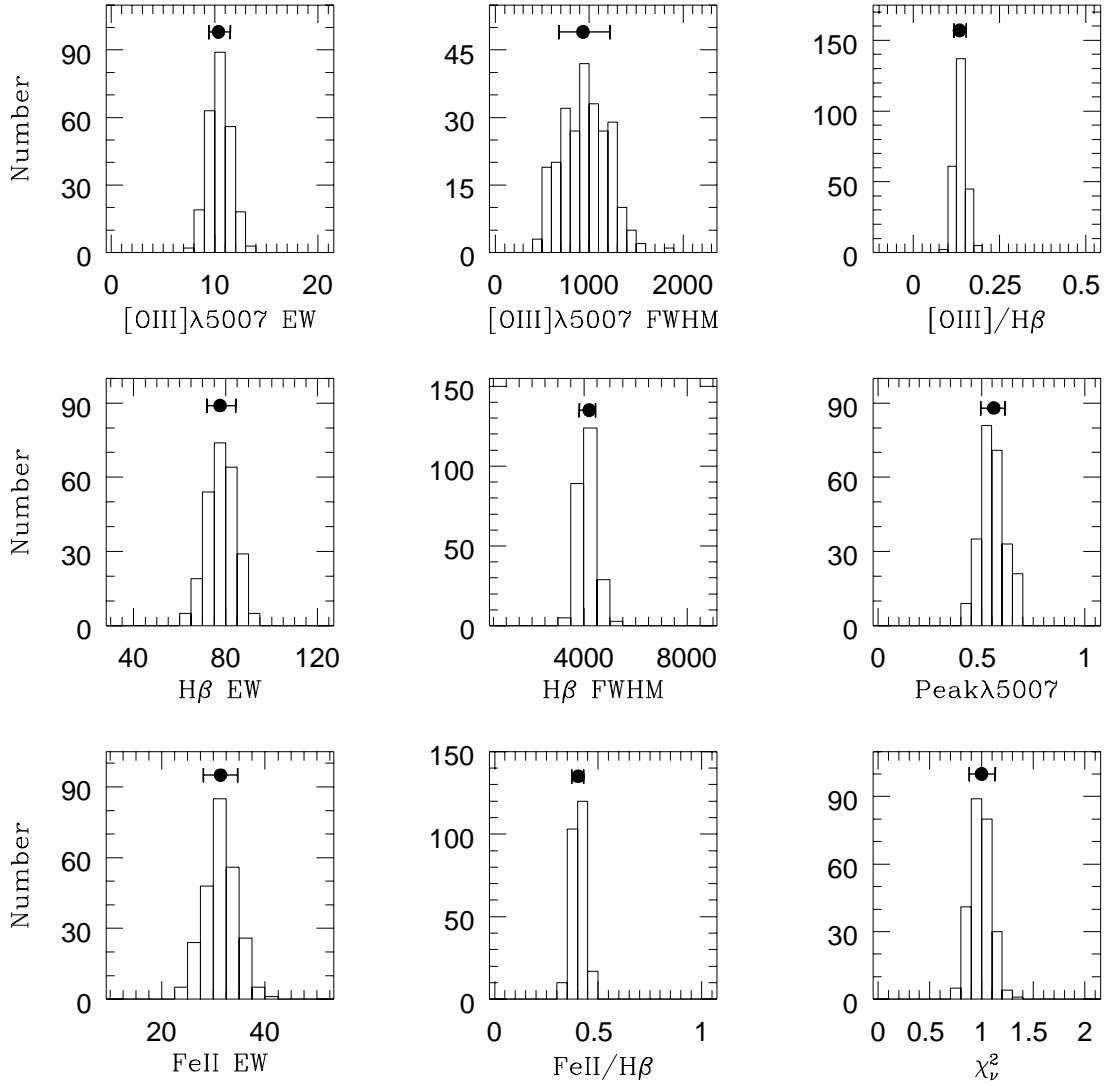


Fig. 3.— The Monte Carlo error distributions for minimized χ^2 best fits to 250 random synthetic representations of PG1247+267. The nine boxes represent eight of the parameters that we measured for each QSO, plus the reduced chi-squared χ^2_{ν} best fit parameter. The solid circle above each parameter distribution represents the value measured from the best fit to the real data, while the right and left 1σ error bars are calculated from the error distributions.

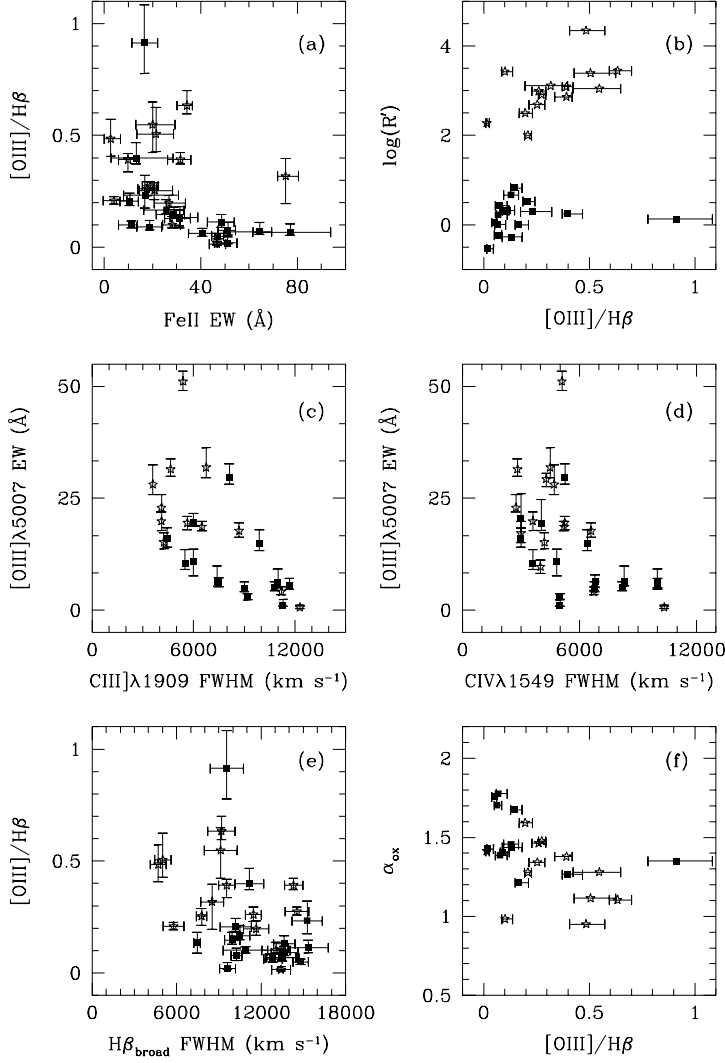


Fig. 4.— The significant correlations with the strength of [O III]λ5007 emission: (a) negative [O III]/Hβ to Fe II EW; (b) positive [O III]/Hβ to log(R'); (c) negative [O III] EW to C III]λ1909 FWHM; (d) negative [O III] EW to C IVλ1549 FWHM; (e) negative [O III]/Hβ to broad Hβ FWHM; and (f) negative [O III]/Hβ to α_{ox} . Solid squares are RQQs, while open stars are RLQs.

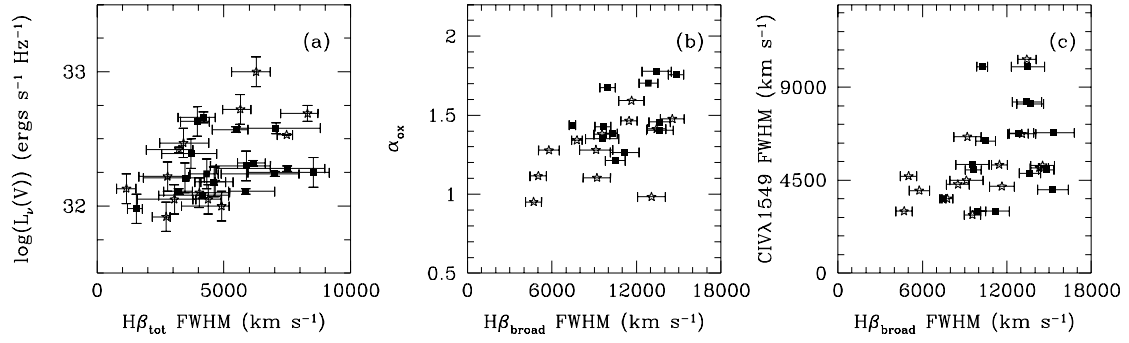


Fig. 5.— The significant positive correlations with the width of $H\beta$ emission: (a) total $H\beta$ FWHM to $L_\nu(V)$; (b) broad $H\beta$ FWHM to α_{ox} ; and (c) $H\beta$ FWHM to C IV $\lambda 1549$ FWHM. Solid squares are RQQs, while open stars are RLQs.

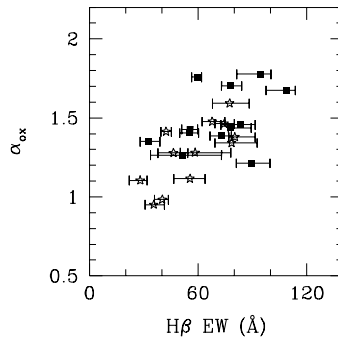


Fig. 6.— The significant positive correlation between H β EW and α_{ox} . Solid squares are RQQs, while open stars are RLQs.

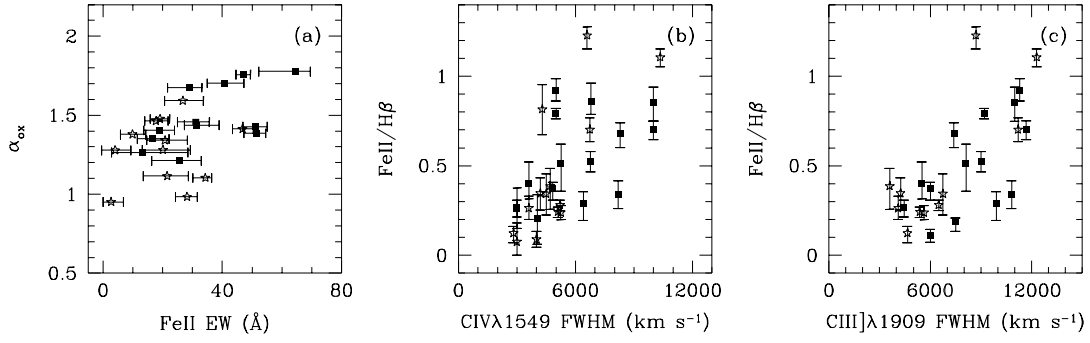


Fig. 7.— The significant positive correlations with the strength of optical Fe II emission: (a) Fe II EW to α_{ox} ; (b) Fe II/H β to C IV λ 1549 FWHM; and (c) Fe II/H β to C III] λ 1909 FWHM. Solid squares are RQQs, while open stars are RLQs.

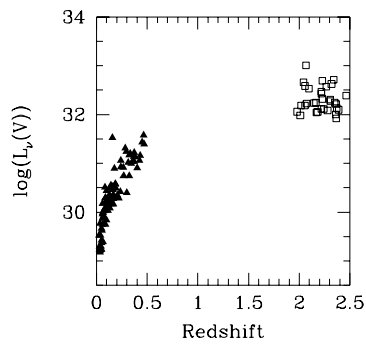


Fig. 8.— The Hubble Diagram for the combined sample of 87 low redshift QSOs from BG92 (solid triangles) and our 32 high redshift QSOs (open squares). The luminosity densities (in units of $\text{ergs s}^{-1} \text{Hz}^{-1}$) were calculated adopting $H_0 = 50 \text{ km s}^{-1} \text{Mpc}^{-1}$ and $q_0 = 0.1$.

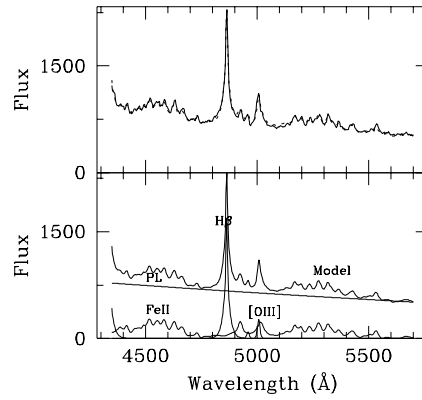


Fig. 9.— Rest-frame spectrum of a representative QSO (PG1404+226) from the low redshift sample of BG92, with its minimized χ^2 best fit model (dashed line) in top panel. The lower panel shows the model (bold line) with its H β , [O III], Fe II and power-law components.

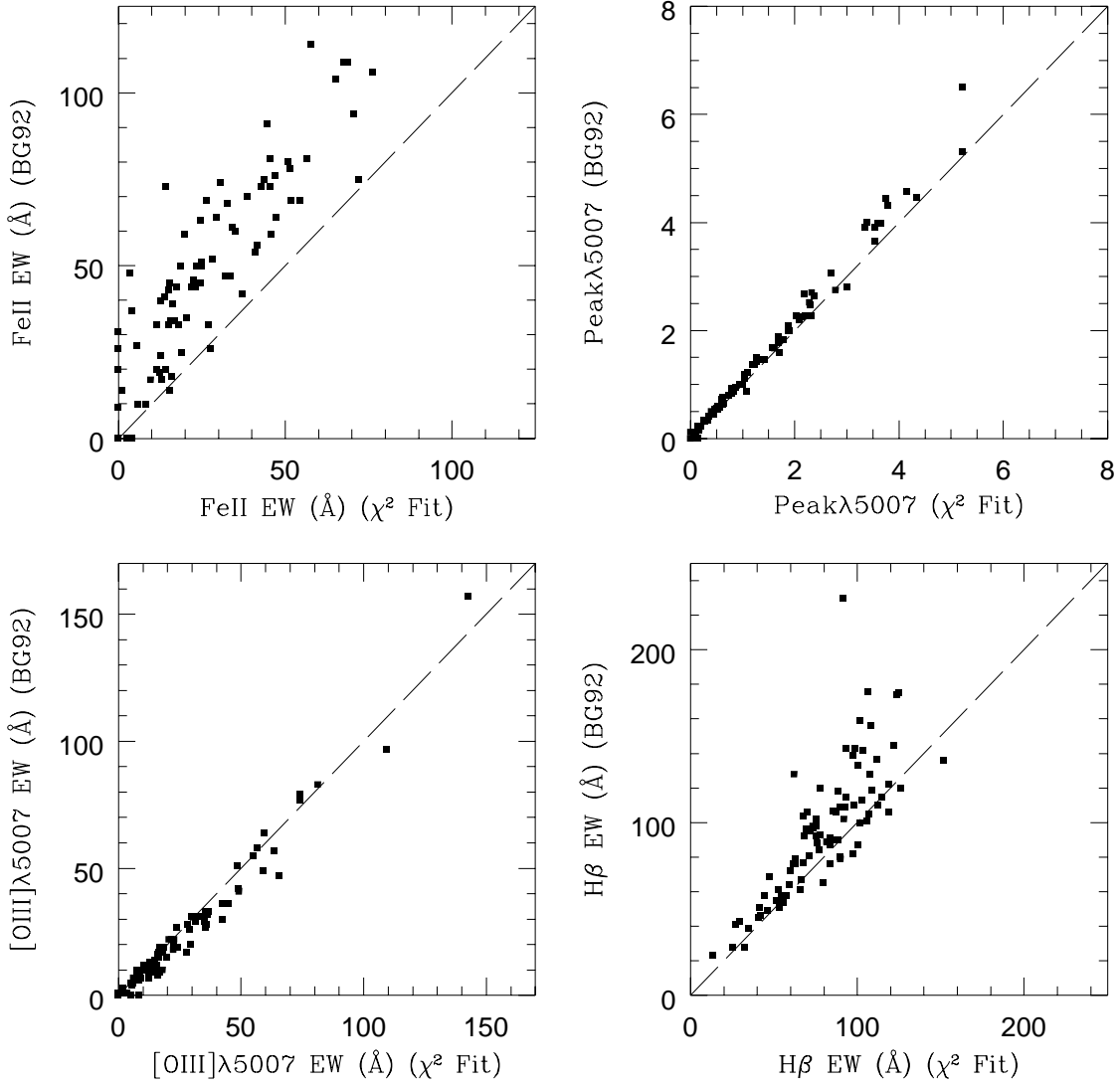


Fig. 10.— Comparison between our minimized χ^2 best fit derived values versus the published BG92 results for the EWs of [O III], and H β , the *relative* EW of optical Fe II, and the Peak λ 5007 parameter.

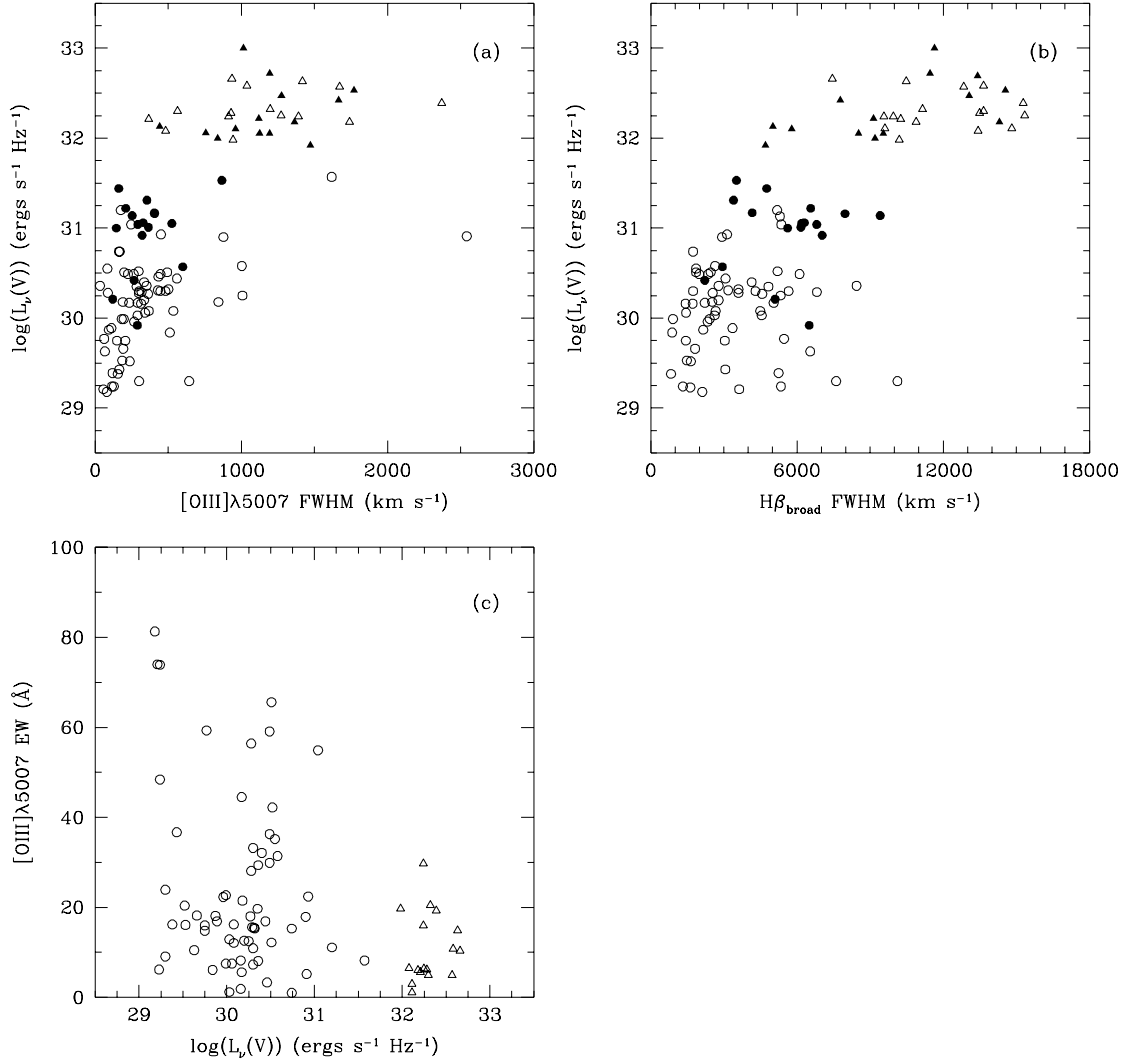


Fig. 11.— The strong luminosity dependencies of the combined low redshift (circles) and high redshift (triangles) $0 < z < 2.5$ sample for (a) rest-frame [O III]λ5007 FWHM, and (b) rest-frame broad Hβ FWHM. Solid symbols are RLQs, while open symbols are RQQs. The Baldwin Effect for the [O III]λ5007 line in the (c) RQQ only subsample.

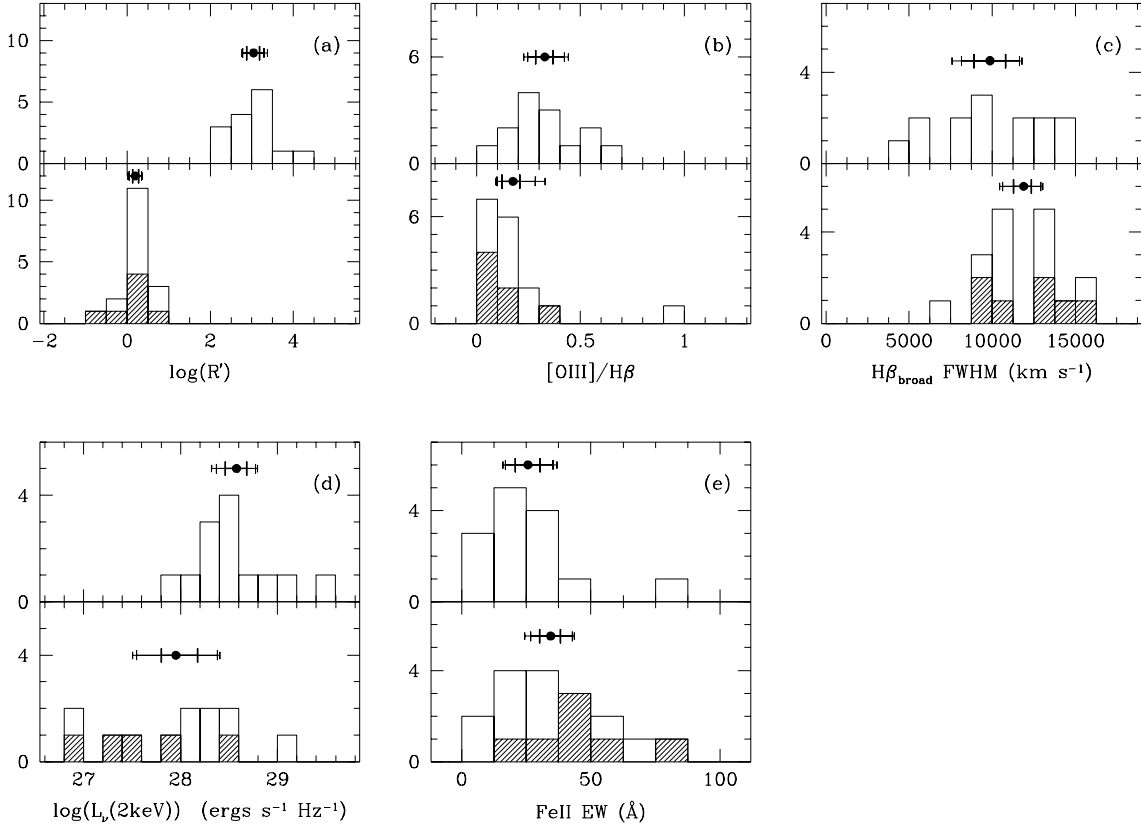


Fig. 12.— The RLQ (upper panel) and RQQ (lower panel – with shaded BALQSO subset over-plotted) subsample distributions: (a) $\log(R')$; (b) $[O\ III]/H\beta$; (c) broad $H\beta$ FWHM; (d) $\log(L_\nu(2\text{keV}))$; and (e) Fe II EW. The vertical axis gives the number per bin. The bin sizes are approximately $2\langle\sigma\rangle$ from the Monte Carlo error analysis. The mean of each panel’s distribution is plotted (solid circle) along with the corresponding right and left $1 - 3\sigma$ uncertainties.